

A thermoacoustic-Stirling heat engine: Detailed study

S. Backhaus and G. W. Swift

*Condensed Matter and Thermal Physics Group, Los Alamos National Laboratory, Los Alamos,
New Mexico 87545*

(Received 29 May 1999; accepted for publication 16 February 2000)

A new type of thermoacoustic engine based on traveling waves and ideally reversible heat transfer is described. Measurements and analysis of its performance are presented. This new engine outperforms previous thermoacoustic engines, which are based on standing waves and intrinsically irreversible heat transfer, by more than 50%. At its most efficient operating point, it delivers 710 W of acoustic power to its resonator with a thermal efficiency of 0.30, corresponding to 41% of the Carnot efficiency. At its most powerful operating point, it delivers 890 W to its resonator with a thermal efficiency of 0.22. The efficiency of this engine can be degraded by two types of acoustic streaming. These are suppressed by appropriate tapering of crucial surfaces in the engine and by using additional nonlinearity to induce an opposing time-averaged pressure difference. Data are presented which show the nearly complete elimination of the streaming convective heat loads. Analysis of these and other irreversibilities show which components of the engine require further research to achieve higher efficiency. Additionally, these data show that the dynamics and acoustic power flows are well understood, but the details of the streaming suppression and associated heat convection are only qualitatively understood. © 2000 Acoustical Society of America.

[S0001-4966(00)00206-X]

PACS numbers: 43.35.Ud [HEB]

INTRODUCTION

Since their invention in 1815, Stirling engines and refrigerators have shown great promise as commercial heat engines.¹ Much of this promise is due to the Stirling cycle's inherent reversibility, and therefore, its high thermal efficiency. Despite this promise, the drawback of Stirling engines has always been the need for multiple sliding seals capable of withstanding high pressure and many cycles without failure. Recent advances in Stirling technology include free-piston machines, the use of linear alternators and motors, and orifice pulse tube refrigerators.² Unfortunately, these advances did not completely eliminate the unreliability and high cost of sliding seals.

The Fluidyne engine³ was the first attempt to totally eliminate sliding seals, by using U-tube liquid pistons. Unfortunately, this solution is limited to low frequency by the high mass of the liquid pistons. Ceperley also attempted to totally eliminate sliding seals.⁴⁻⁶ He realized that a traveling acoustic wave propagating through a regenerative heat exchanger (regenerator) undergoes a thermodynamic cycle similar to the Stirling cycle. As the wave travels up the temperature gradient through the regenerator (i.e., from ambient temperature toward high temperature), it carries the gas in the regenerator through a sequence of displacement toward higher temperature, depressurization, displacement toward lower temperature, and pressurization. The gas experiences thermal expansion during the displacement toward higher temperature and thermal contraction during the displacement toward lower temperature, so that acoustic power is amplified as it travels toward higher temperature; this is the source of the engine's net work. Simultaneously, the gas gains entropy from the regenerator solid during the depressurization and loses entropy to the solid during pressurization, so that the two displacement processes result in a net convection of

entropy down the temperature gradient; this is the mechanism by which the engine extracts heat from the high-temperature heat source and rejects heat to the ambient-temperature heat sink.

Ceperley's experimental engine was not able to amplify acoustic power. Much later, Yazaki *et al.*⁵ first demonstrated such an engine, but at low efficiency. Ceperley and Yazaki realized that this was due to the low acoustic impedance of the working gas, which caused large viscous losses resulting from high acoustic velocities.⁶ Also, they did not anticipate the presence of several forms of acoustic streaming, including "Gedeon streaming" which occurs whenever a traveling-wave component is present⁷ and "Rayleigh streaming" which is due to boundary-layer effects in the gas space that provides the thermal buffer for the hot heat exchanger.⁸ Although Gedeon streaming has been detected experimentally,^{9,10} we have found no published description of a systematic method to suppress it.

Another engine without sliding seals is a standing-wave thermoacoustic engine.¹¹ Many engines of this type have been built, but because they are based on an intrinsically irreversible thermodynamic cycle their thermal efficiency (ratio of acoustic power produced to heater power consumed) has thus far been limited to 0.20.¹²

This paper describes a Stirling-cycle based thermoacoustic engine, which was introduced briefly in an earlier paper.¹³ Since it employs the inherently reversible Stirling cycle, this engine's thermal efficiency can easily surpass that of standing-wave engines. To create the traveling-wave phasing and high acoustic impedance in the regenerator desired by Ceperley,⁶ the engine uses a compact acoustic network. Unchecked, both Gedeon and Rayleigh streaming would seriously degrade the thermal efficiency of the engine. Gedeon streaming is suppressed by using hydrodynamic end effects

which produce an opposing time-averaged pressure difference. Rayleigh streaming is suppressed through the use of an appropriately tapered thermal buffer tube⁸ (referred to as a pulse tube in the context of orifice pulse tube refrigerators). With the heat loads due to both types of streaming reduced to an acceptable level, this engine has demonstrated a thermal efficiency of 0.30 which is more than 50% higher than any previous thermoacoustic engine. For comparison, typical thermal efficiencies of internal combustion engines are 0.25 for gasoline and 0.40 for diesel.¹⁴

The next section describes the engine and its construction in detail. The following section presents two simplified models of the engine which provide some intuition about the creation of traveling-wave phasing with high acoustic impedance and how various components of the engine affect these properties. Then, preliminary measurements are shown which demonstrate our good understanding of the acoustic network and our qualitative understanding of the effects and suppression of acoustic streaming. Finally, data on the performance of the engine and on the various loss mechanisms are presented. These data demonstrate a quantitative understanding of the dynamics and acoustic power flows and a qualitative understanding of the acoustic streaming and associated heat convection.

I. APPARATUS

Scale drawings of the apparatus used in these measurements are shown in Fig. 1(a) and (b). Essentially, it is composed of a 1/4-wavelength resonator filled with 30-bar helium. The torus-shaped section contains the heat exchangers, regenerator and other duct work necessary to force the helium to execute the Stirling cycle.¹⁵ The rest of the hardware past the resonator junction forms the resonator and variable acoustic load.¹⁶

Near the top of the torus is the main cold heat exchanger. It is of shell-and-tube construction consisting of 299 2.5-mm inside-diameter, 20-mm-long stainless-steel tubes welded into two 1.6-mm-thick stainless-steel plates. The wall thickness of the tubes is 0.7 mm. The diameter of the heat exchanger, measured from the outer edge of the tubes on the periphery, is 9.5 cm. The tubes, which are parallel to the acoustic displacement, carry the helium gas. They are cooled by chilled water ($\approx 15^\circ\text{C}$) passing through the shell. At high amplitude, the peak-to-peak gas displacement is roughly equal to the length of the tubes and the typical Reynolds number in the tubes is 3000.

Below the main cold heat exchanger is the regenerator, made from a 7.3-cm-tall stack of 120-mesh stainless-steel screen machined to a diameter of 8.89 cm. The diameter of the screen wire is $65\ \mu\text{m}$. The randomly stacked screens are contained within a thin-wall stainless-steel can for ease of installation and removal. On each end, three 3.2-mm-thick stainless-steel ribs are welded to the can to hold the screen axially and to provide spacing between the regenerator and adjacent heat exchangers. At the upper end, this spacing allows the flow to spread over the entire regenerator cross section after exiting the narrow passages of the main cold heat exchanger. Based on the total weight of screen in the

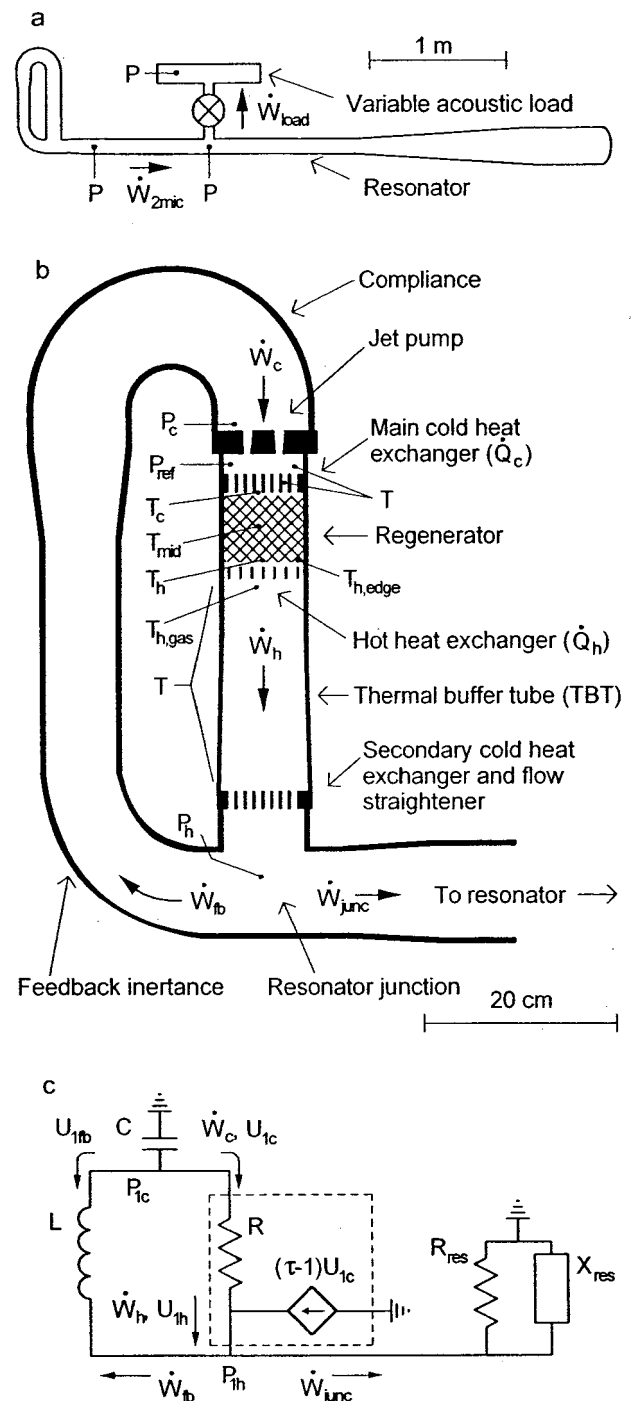


FIG. 1. (a) Scale drawing of the engine, resonator and variable acoustic load (load is not to scale). The 1/4-wavelength resonator is filled with 30-bar helium. The pressure antinode is located near the top of the torus section, and the node is near the inlet to the large cone. The variable acoustic load consists of an adjustable globe valve attached to a 2.2 l tank. (b) Scale drawing of the torus section. Locations labeled with T or P indicate where temperature and pressure are measured. The pressure measurement location labeled P_{ref} is the reference location for measurements of acoustic amplitude in the engine. (c) Lumped-element model of the engine. All elements in the torus are much shorter than 1/4 wavelength. Therefore, they can be modeled as lumped elements. Subscripts in (c) correspond to the locations in (b). The regenerator and adjacent heat exchangers are modeled by the elements inside the dashed box. See text for description of the model.

regenerator, we calculate its volume porosity $\phi \approx 0.72$ and the hydraulic radius $r_h \approx 42\ \mu\text{m}$.¹⁵ This is smaller than the helium's thermal penetration depth δ_κ , which varies from $140\ \mu\text{m}$ to $460\ \mu\text{m}$ through the regenerator. The pressure

vessel around the regenerator, which is made from Inconel 625 (ASTM B446-Grade 2), has a wall thickness of 4.0 mm. This alloy was chosen for its high tensile strength at elevated temperatures as well as its comparatively low thermal conductivity;¹⁷ the heat leak carried by the pressure-vessel wall would have been about a factor of 3 higher if we had used 316H stainless steel.

The lower end of the regenerator abuts the hot heat exchanger. It consists of a 0.64-cm-wide by 3.5-m-long Ni-Cr ribbon wound zigzag on an alumina frame. The ribbon is divided into 3 equal-length segments of 4.0 Ω each and driven with 208-V three-phase power in a delta configuration. Electrical leads enter perpendicular to the pressure-vessel axis just below the hot heat exchanger. This location is chosen so as to not disturb the flow in the thermal buffer tube. Power flowing into the hot heat exchanger is measured using a commercial wattmeter with a 0.2% accuracy.¹⁸ Up to 5.5 kW is supplied to the heat exchanger with the surrounding gas at 725 °C.

The thermal buffer tube (TBT) is a tapered, 24-cm-long open cylinder made of the same Inconel 625. It provides a thermal buffer between the hot heat exchanger and room temperature. Its inner diameter is much larger than the helium's thermal penetration depth, and its length is much greater than the peak-to-peak gas displacement (4 cm) at high amplitudes. The inside surface is polished to a 1- μ m finish to ensure that the surface roughness is much less than the viscous and thermal penetration depths. The wall thickness is 4.0 mm for the entire length. The upper 8.0 cm of the TBT is a straight cylinder while the lower 16.0 cm is flared with a 1.35° half-angle taper. This shape is used to minimize boundary-layer driven streaming (Rayleigh streaming) in the TBT.⁸

At the lower end of the TBT is a flow straightener made of five layers of 22-mesh copper screen with a wire diameter of 0.4 mm. It ensures that the flow entering the bottom of the TBT is spatially uniform, not a jet flow due either to the geometry of the secondary cold heat exchanger or to flow separation at the resonator junction. A jet flow would cause streaming within the TBT to convect heat from the hot heat exchanger. Before the flow straightener was installed, up to 1 kW of heat was convected away in this fashion.

Next, a secondary, water-cooled, shell-and-tube heat exchanger anchors the lower end of the TBT at room temperature. It contains 109 4.6-mm inside-diameter, 10-mm-long stainless-steel tubes welded into two 1.6-mm-thick stainless-steel plates. If both forms of streaming are suppressed, this heat exchanger only intercepts the leak down the TBT wall and radiation from the hot heat exchanger, so it can be made from short, large-diameter tubes.

Several 1.6-mm-diameter type-K thermocouples allow the measurement of temperatures throughout the Stirling section of the engine. Starting at the top of Fig. 1(b), two thermocouples are located near the main cold heat exchanger. One is freely suspended within one of the tubes and the other is located in the helium, 1 cm above the heat exchanger assembly. Also, there are two thermocouples (not shown in the figure) in the inlet and outlet chilled water streams supplying this heat exchanger. These four thermocouples allow

us to assess the performance of this heat exchanger by measuring the heat load on the heat exchanger (via the temperature rise of the chilled water) and the temperature defect between the helium and the chilled water. Next are four thermocouples in contact with the regenerator screen bed. The first extends through a tube of the main cold heat exchanger and is pressed against the center of the regenerator's cold end. The other three pass through the pressure-vessel wall and are inserted into tight-fitting pockets drilled into the regenerator. Of these three, two are centered radially with one near the hot end and the other centered axially. The last thermocouple is near the hot end, but its pocket is only drilled 1 cm into the regenerator. The three radially centered thermocouples allow the measurement of the axial temperature profile within the regenerator. This profile is important in detecting and eliminating Gedeon streaming. The two thermocouples near the hot end allow measurement of the radial temperature profile. We believe that vigorous Rayleigh or jet-driven streaming in the TBT causes unequal heating of the hot face of the regenerator. In a previous version of this engine in which there was no attempt to suppress either type of streaming, up to 100 °C differences were measured between the center and edge of the regenerator's hot face. In the present engine, up to 90 °C differences were measured before the flow straightener was installed; a maximum of 30 °C was measured after the installation. Finally, there are eight thermocouples held against the outer wall of the TBT by set screws, spaced every 2.5 cm. After the bulk of the Gedeon streaming is suppressed, the axial temperature profile measured by these thermocouples is used to detect the presence of either Rayleigh or jet-driven streaming.

Clockwise farther around the torus are the resonator junction, feedback inertance, and compliance. The junction is a standard-wall, 3 1/2-in. nominal, stainless-steel tee. The inside diameter is roughly 9.0 cm. The feedback inertance consists of three separate sections of piping. The first section is a 3 1/2-in. to 3-in. nominal, long-radius reducing elbow. The centerline length of the elbow is 20.9 cm, and the final inside diameter of the elbow is 7.8 cm. All burrs and irregularities on the inside of the elbow have been removed by grinding and filing. The next section is a 3-in. nominal, stainless-steel pipe 25.6-cm long. The inside diameter of this pipe is honed to 2- μ m finish, to minimize viscous loss at high amplitudes. This segment of pipe includes a pressure-balanced sliding joint (not shown) which allows for the thermal expansion of the TBT and regenerator case. When the hot temperature rises from 25 °C to 725 °C, these components expand roughly 3 mm; without the sliding joint, the resulting stress would cause the hot components to distort. The last section of the inertance is a machined cone that adapts the 3-in. nominal pipe to the compliance. Its initial and final inside diameters are 7.8 cm and 10.2 cm, and its length is 10.2 cm, giving a taper angle of 13.5°. The gradual cross-sectional area changes, gentle bends, and smooth surfaces are used to minimize dissipation due to flow separation¹⁹ and viscosity in the feedback inertance. The compliance consists of two 4-in. nominal, short-radius 90° elbows made from carbon steel. The inner surface of the elbows is sandblasted to remove a protective layer of paint.

Although this treatment left the surface quite rough, the acoustic velocities in the compliance are low, so the rough surface should not affect the dissipation significantly. The internal volume of the compliance is 2830 cm³, measured by filling it with a known volume of water.

Between the compliance and the main cold heat exchanger is a device we have termed a “jet pump,”²⁰ which stops Gedeon streaming. We will reserve discussion of this component until the section on streaming.

The resonator, which joins with the torus at the junction between the TBT and feedback duct, consists of three sections. The first section is a machined cone that adapts the 3 1/2-in. nominal tee to a 4-in. nominal, carbon-steel pipe. The initial and final inside diameters of the cone are 9.0 cm and 10.2 cm, and the length is 10.2 cm resulting in a 6.8° taper angle. The small angle is used to prevent flow separation at the walls of the cone.¹⁹ The main section of the resonator is a 1.90-m length of 4-in. nominal, carbon-steel pipe. The inside diameter of the pipe is 10.2 cm and is honed to a 2-μm surface finish. The resonator diameter is enlarged over the engine diameter to reduce the acoustic velocities near the velocity antinode at the end of the main resonator section. The increase in surface area tends to increase the dissipation, but the reduction in velocity is more important at high amplitude where the acoustic losses grow as the cube of the amplitude.²¹ The final section of the resonator includes a 7° cone which enlarges the inside diameter of the resonator from 10.2 cm to 25.5 cm over a length of 1.22 m. The large end of the cone is closed with a 25.5-cm-diameter pipe with an approximate length of 52 cm, terminating in a 2:1 ellipsoidal cap. The main section of the resonator has three ports of 1.6-cm diameter. Two of these are located near the ends and the third is in the center. A variable, RC-type acoustic load¹⁶ can be attached to either of the two ports nearest the resonator junction. The fill line is connected to the port nearest the 7° cone. Two piezoresistive pressure sensors²² located in the resonator and a third in the variable acoustic load allow two-microphone power measurements of \dot{W}_{2mic} and \dot{W}_{load} .¹⁶ All acoustic pressure measurements are made with a lock-in amplifier using the measured acoustic pressure immediately above the main cold heat exchanger as a reference signal.

In addition to the pressure sensors in the resonator, three additional pressure sensors are located in the torus: between the compliance and jet pump, between the jet pump and main cold heat exchanger, and at the resonator junction. Additionally, a differential pressure sensor is placed across the jet pump. A Bourdon-tube gauge connected through a fine capillary is used to measure the mean pressure in the engine.

II. SIMPLIFIED MODELS

Figure 1(c) shows the simplest lumped-element model of the engine that captures all the most important features. Each component of the engine is replaced with its idealized lumped-element equivalent.²³ The resonator is modeled as resistive and reactive impedances in parallel, R_{res} and iX_{res} , respectively. R_{res} is controlled by the resonator dissipation and the variable acoustic load. At this point, no distinction is

made between these two mechanisms. Under the normal operating conditions $X_{res} \ll R_{res}$. The impedances of the regenerator R and feedback inertance L are much smaller than that of the compliance C . Therefore, ω is determined primarily by the resonance condition between X_{res} and the compliance: i.e., $X_{res}(\omega) \approx 1/\omega C$.

We use the conventional counterclockwise phasor notation,¹¹ so that time-dependent variables are expressed as

$$\xi(t) = \xi_m + \text{Re}[\xi_1 e^{i\omega t}], \quad (1)$$

with the mean value ξ_m real, and with ξ_1 complex to account for both the magnitude and phase of the oscillation at angular frequency ω . The acoustic pressure and volumetric velocity (i.e., volume flow rate) are represented by $p_{1,x}$ and $U_{1,x}$ at the points in Fig. 1(b) and (c) labeled with the subscript x . For example, $p_{1,h}$ is the complex amplitude of the acoustic pressure oscillation at the location labeled with a subscript h in Fig. 1(b), between the regenerator and hot heat exchanger.

Following Ceperley,⁴ we model the regenerator and adjacent heat exchangers by the resistance and volumetric-velocity source inside the dashed box. The resistance is due to viscous flow in the tightly-spaced screen bed that forms the regenerator.²⁴ The volumetric-velocity source is due to the temperature profile. The mean temperature T_m changes axially through the regenerator, and hence the mean density ρ_m changes according to $\rho_m \propto 1/T_m$. To enforce the conservation of first-order mass flux, $\rho_m U_1 = \text{const}$ throughout an ideal regenerator with negligible internal compliance, the volumetric velocity U_1 must grow as T_m . Therefore, the volumetric velocity $U_{1,h}$ at the hot end of the regenerator would ideally be $\tau U_{1,c}$, where $\tau = T_h/T_c$ is the ratio of absolute temperatures at the regenerator ends. The volumetric-velocity source is set to $(\tau - 1)U_{1,c}$ to enforce this condition.

The study of this simple model provides some basic insights into the operation of the engine. We have $i\omega L U_{1,fb} = U_{1,c} R$ and $U_{1,c} + U_{1,fb} = -i\omega C p_{1,c}$. Eliminating $U_{1,fb}$ and solving for $U_{1,c}$, we find

$$U_{1,c} = \frac{\omega^2 LC}{R} \frac{p_{1,c}}{1 + i\omega L/R}. \quad (2)$$

If the magnitude of the impedance of the feedback inertance ωL is small compared with the resistance R of the regenerator, $p_{1,c}$ and $U_{1,c}$ are nearly in phase corresponding to the traveling-wave phasing necessary for efficient regenerator operation.⁴ The magnitude of $U_{1,c}$ is controlled by the magnitudes of all three impedances: R , ωL and $1/\omega C$. The magnitude of the volumetric velocity passing through the parallel combination of the feedback inertance and the regenerator is given by the magnitude of the volumetric velocity into the compliance, or $\omega C p_{1,c}$. As the compliance becomes larger, this volumetric velocity grows as does $U_{1,c}$. Since $U_{1,c}/U_{1,fb} = i\omega L/R$, the volumetric velocity in the feedback inertance is always 90° out of phase from that in the regenerator, with increasing volumetric velocity through the regenerator as the impedance of the inertance increases relative to the regenerator resistance. The ability to tune the magni-

tude of the volumetric velocity in the regenerator is equivalent to tuning its power output. This degree of freedom is useful in the design process when trading off losses in the regenerator against resonator and feedback loss during optimization of the entire system.

Next, it is useful to look at the time-averaged acoustic power flows $\dot{W} = \text{Re}[p_1 \tilde{U}_1]/2$ at various points in the engine. Using Eq. (2), the time-averaged power flow into the regenerator is given by

$$\dot{W}_c \approx \frac{|p_{1,c}|^2}{2} \frac{\omega^2 LC}{R}, \quad (3)$$

where we have dropped terms of order $(\omega L/R)^2$. Neither the compliance nor inertance absorb or generate time-averaged power. This implies that \dot{W}_c is the power fed back through the inertance, i.e., $\dot{W}_c = \dot{W}_{fb}$. Since the impedance of the parallel combination of the regenerator and feedback inertance is small compared to that of the compliance or resonator, $p_{1,h} \approx p_{1,c}$. Therefore, the time-averaged power flowing out of the hot end is then given by

$$\dot{W}_h \approx \tau \dot{W}_c. \quad (4)$$

By conserving the time-averaged power flow at the resonator junction, the resonator is found to absorb an amount of power given by

$$\dot{W}_{\text{junc}} \approx (\tau - 1) \dot{W}_c. \quad (5)$$

To determine τ , \dot{W}_{junc} is expressed in terms of R_{res} and substituted into Eq. (5). Using Eq. (3), τ is given by

$$\tau \approx 1 + \frac{R}{\omega^2 LCR_{\text{res}}}. \quad (6)$$

In an ideal regenerator that uses an ideal gas, $\dot{W}_h = \dot{Q}_h$ where \dot{Q}_h is the heat input from the hot heat exchanger.²⁵ Substituting Eqs. (3) and (4), $|p_{1,c}|^2$ is found to be

$$|p_{1,c}|^2 \approx \frac{2R}{\tau \omega^2 LC} \dot{Q}_h. \quad (7)$$

Equations (6) and (7) show how the operating point of the engine is set by the external controls. Setting R_{res} , by adjusting the variable acoustic load, sets T_h by fixing τ . With T_h determined, the acoustic amplitude is set by adjusting the heat input \dot{Q}_h .

At fixed acoustic amplitude, Eq. (3) shows that power input to the regenerator only depends on ω and the geometry of the inertance, compliance, and regenerator. Therefore, for a simple fixed-amplitude point of view, a constant power \dot{W}_c circulates around the torus. This power is amplified by the temperature gradient in the regenerator, and the added power $(\tau - 1) \dot{W}_c$ is delivered to the resonator. If \dot{W}_{junc} is increased at *fixed acoustic amplitude*, the ‘‘power gain’’ of the regenerator, i.e., τ , must grow.

The results of this section, in particular Eq. (2), separate this engine from that originally envisioned by Ceperley.⁴ A figure of merit for a regenerator in a traveling-wave engine is $\beta = \dot{W}_c / \dot{E}_{\text{vis}}$ where \dot{E}_{vis} is the time-average power dissipated in the regenerator due to viscosity. Using $\dot{E}_{\text{vis}} \approx R |U_{1,c}|^2/2$

and $\dot{W}_c = |p_{1,c}| |U_{1,c}|/2$ (assuming nearly traveling-wave phasing), this figure of merit can be rewritten $\beta \approx |Z|/R$ where Z is the acoustic impedance in the regenerator. If a pure traveling wave is used, i.e., one with $Z = \rho_m c/A$ where c is the speed of sound and A is the cross-sectional area of the waveguide containing the wave, $\beta \approx 1$ indicating that the regenerator is dissipating nearly all of the acoustic power it is trying to amplify. Ceperley⁶ realized that viscous dissipation in the regenerator is a serious problem, but his proposed solution involved placing the regenerator in a looped resonator at least one wavelength long.^{5,6} In an engine of this type, the viscous dissipation associated with the large amount of resonator surface area would cause a large reduction in efficiency. Also, it is not clear how to control the phase between $p_{1,c}$ and $U_{1,c}$ or $|p_{1,c}/U_{1,c}|$. The engine described in this article avoids much of the resonator dissipation by using an acoustic network that is much shorter than 1/4 of a wavelength. Also, the magnitudes of R , L , and C are designed to create $|Z|$ which is 15 to 30 times $\rho_m c/A$ and $p_{1,c}$ roughly in phase with $U_{1,c}$, thus avoiding large viscous losses in the regenerator.

The simplified model presented above provides an intuitive picture of how the power flows are distributed, how T_h and $p_{1,c}$ are determined, and what sets ω . One place where more accuracy is desired is the prediction of $U_{1,c}$ and $U_{1,h}$. These two phasors determine whether the acoustic wave has the desired traveling-wave phasing. Detailed control of this phasing is advantageous as it allows the maximum acoustic power flow with the minimum acoustic velocity and therefore minimum viscous loss.² It is not intuitively obvious how these phasors are influenced by the impedances of the components, and it turns out they can be very sensitive to non-ideal behavior of the various components in the torus. To analyze these phenomena, Fig. 2(b) shows a detailed impedance model of the engine, which includes more of the acoustic elements in the engine, provides a more complete model of the regenerator, and includes the nonideal behavior of some the acoustic elements.

The regenerator is more complex than in the lumped-element model presented above. The volumetric-velocity gain occurs in a distributed manner. Therefore, the hotter sections of the regenerator have larger volumetric velocities and larger pressure drops. The pressure drops on the hot end are enhanced further due to the temperature dependence of the viscosity. Also, the porosity of the regenerator gives it compliance. These two effects are shown in the distributed regenerator model of Fig. 2(a). The regenerator of length l is split into $N = l/\Delta x$ segments, each of length Δx and spanning a temperature difference ΔT_n . With an ideal gas as the working fluid, each segment of regenerator has an isothermal compliance $\Delta C = C_0 \Delta x/l$ independent of temperature, where $C_0 = \phi S l/p_m$ and ϕ and S are the volume porosity and cross-sectional area of the regenerator. Across each segment, the volumetric velocity changes due to the temperature increase and the compliance, i.e., $U_{1,n+1} - U_{1,n} = U_{1,n} \Delta T_n / T_{m,n} - i \omega \Delta C p_{1,n}$. Dividing through by Δx and letting $\Delta x \rightarrow 0$ yields a differential equation for $U_1(x)$,

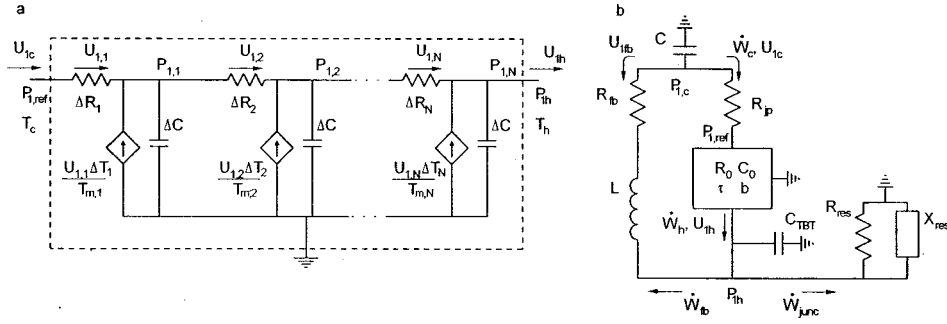


FIG. 2. (a) Distributed model of the regenerator. Each of the N sections spans ΔT_n and represents a length Δx of the regenerator. The resistances ΔR_n differ due to the temperature dependence of viscosity. The compliances are due to the void volume in the regenerator. (b) Detailed impedance model of the thermoacoustic-Stirling engine. The distributed model of the regenerator is included as the three-terminal network. Resistors R_{fb} and R_{jp} represent the resistances due to viscous and minor losses in the feedback inductance and jet pump respectively. C_{TBT} represents the compliance of the thermal buffer tube. Subscripts in (b) correspond to the locations in Fig. 1(b).

$$\frac{dU_1}{dx} = \frac{U_1}{T_m} \frac{dT_m}{dx} - i\omega(C_0/l)p_1(x). \quad (8)$$

Each segment of regenerator also has a resistance given by $\Delta R_n = (R_0 \Delta x / l)(T_{m,n} / T_c)^b$, where $R_0 \approx 6\mu_c l / S r_h^2$ is the low-Reynolds-number-limit flow resistance of the regenerator when its entire length is at temperature T_c . At high amplitude, R_0 would increase by up to 50%, but this effect is not included in the model. The factor $(T_{m,n} / T_c)^b$ accounts for the temperature dependence of the viscosity $\mu(T) = \mu_c (T / T_c)^b$. The pressure drop across each segment is given by $p_{1,n} - p_{1,n-1} = -\Delta R_n U_{1,n}$. Dividing through by Δx and letting $\Delta x \rightarrow 0$ yields a differential equation for $p_1(x)$,

$$\frac{dp_1}{dx} = -\frac{R_0}{l} \left(\frac{T_m}{T_c}\right)^b U_1(x). \quad (9)$$

In the limit of low amplitude and $r_h \ll \delta_c$, Eqs. (8) and (9) are consistent with Eqs. (12) and (42) of Ref. 26.

Under typical operating conditions, the pressure drop across the regenerator $|\Delta p_{1,regen}| = |p_{1,ref} - p_{1,h}| \approx 0.1 |p_{1,ref}|$. Therefore, an approximate solution of Eqs. (8) and (9) is obtained by setting $p_1(x) = p_{1,ref}$ in Eq. (8) and integrating. The result,

$$U_1(x) = \left[1 + (\tau - 1) \frac{x}{l} \right] \times \left\{ U_{1,c} - \frac{i\omega C_0 p_{1,ref}}{\tau - 1} \ln \left[1 + (\tau - 1) \frac{x}{l} \right] \right\}, \quad (10)$$

is then substituted into Eq. (9) and integrated again. In both integrations, $T_m(x)$ is assumed to vary linearly from T_c to T_h . The volumetric velocity at the hot end of the regenerator and the pressure drop are then given by

$$U_{1,h} = \tau \left(U_{1,c} - \frac{i\omega C_0 \ln \tau}{\tau - 1} p_{1,ref} \right), \quad (11)$$

$$\Delta p_{1,regen} = U_{1,c} R_0 \frac{\tau + 1}{2} f(\tau, b) - \frac{i\omega C_0 R_0 p_{1,ref}}{2} g(\tau, b),$$

where f and g are given by

$$f(\tau, b) = \frac{2}{b+2} \left[\frac{\tau^{b+2} - 1}{\tau^2 - 1} \right],$$

$$g(\tau, b) = \frac{2}{b+2} \left[\frac{\tau^{b+2} \ln \tau - (\tau^{b+2} - 1)/(b+2)}{(\tau - 1)^2} \right]. \quad (12)$$

Both of these functions approach 1 as $\tau \rightarrow 1$. Using $b = 0.68$, which is appropriate for helium gas, the calculated pressure drop at $\tau = 3$ is approximately 70% bigger than that calculated with $b = 0$. Equations (11) and (12) for $\Delta p_{1,regen}$ and $U_{1,h}$ in terms of $U_{1,c}$ and $p_{1,ref}$ provide a simple model of a regenerator which includes its distributed properties such as axial temperature dependence and compliance.

The distributed model of the regenerator is included as a three-terminal network in the detailed impedance model of the engine shown in Fig. 2(b). Several new elements are also included. The resistance R_{fb} in the feedback path represents acoustic losses due to both viscous drag and flow separation.¹⁹ The extra resistance R_{jp} appearing on the cold side of the regenerator represents the same type of losses which occur in the jet pump. Finally, the compliance C_{TBT} appearing below the regenerator models the compressibility of the gas in the TBT. A detailed analysis of the model in Fig. 2(b) shows that the volumetric velocity into the cold end of the regenerator is given by

$$U_{1,c} = \frac{p_{1,c}}{R_{fb} + \frac{i\omega L}{R_{St}}} \left[\frac{\omega^2 LC}{R_{St}} \left(1 - \frac{iR_{fb}}{\omega L} \right) + \frac{i\omega R_0 C_0 g}{2R_{St}} \right], \quad (13)$$

where $R_{St} = R_{jp} + R_0(\tau + 1)f/2$ is the effective series resistance of the jet pump and regenerator referred to $U_{1,c}$. In Eq. (13), we have ignored the pressure drop across R_{jp} by taking $p_{1,ref} = p_{1,c}$. This equation provides a more accurate version of the phenomena discussed above than Eq. (2).

Equations (11) and (13) are important in the design of a thermoacoustic-Stirling engine. For efficient regenerator operation, $U_{1,c}$ should lead $p_{1,c}$, and $U_{1,h}$ should lag $p_{1,c}$.² This allows maximum acoustic power flow with the minimum volumetric velocity, and therefore a minimum of viscous loss in the regenerator. Also, for a given $p_{1,c}$, the size of the various components determines the magnitude of $U_{1,c}$ and hence the amount of power flow through the regenerator.

If the engine must drive a very lossy system, the power output of the engine can be increased at the expense of increased regenerator loss, allowing the designer some freedom to balance the losses against one another.

The origin of the dominant part of Eq. (13), $\omega^2 LC p_{1,c}/R_{St}$, is understood by considering the pressure drop across the impedance of the parallel combination of the feedback and regenerator branch, Z_p . Ignoring the compliance in the regenerator branch for the moment, the total volumetric velocity through these two branches is $U_{1,c} + U_{1,fb} = -i\omega C p_{1,c}$. Therefore, the pressure drop $\Delta p_1 = -i\omega C Z_p p_{1,c}$ appears across the temperature-dependent resistance R_{St} of the regenerator branch, giving $U_{1,c} = -i\omega C Z_p p_{1,c}/R_{St}$. If the impedance of the inertance dominates, i.e., $R_{St} \gg \omega L \gg R_{fb}$, then $Z_p \approx i\omega L$. In this case, $U_{1,c} = \omega^2 LC p_{1,c}/R_{St}$ and $U_{1,c}$ is in phase with $p_{1,c}$.

If ωL becomes comparable to either R_{St} or R_{fb} , Z_p rotates into the first quadrant, causing $U_{1,c}$ to lag $p_{1,c}$. This accounts for the $1 - iR_{fb}/(\omega L)$ and $1 + (i\omega L)/R_{St}$ terms in Eq. (13). Even in the most ideal case, i.e., $R_{St} \gg \omega L \gg R_{fb}$, $U_{1,c}$ will at best be in phase with $p_{1,c}$. Some other effect is needed to force $U_{1,c}$ to the desired condition leading $p_{1,c}$. Such an effect is found in the compliance of the regenerator. The oscillating pressure $p_{1,c}$ causes a volumetric-velocity difference of $i\omega C_0 p_{1,c}$ across the regenerator. Only part of this volumetric velocity originates from the cold end of the regenerator, but the fraction that does is responsible for the term $(i\omega C_0 p_{1,c})gR_0/(2R_{St})$ in Eq. (13). This volumetric velocity is proportional to $i p_{1,c}$ and causes $U_{1,c}$ to lead $p_{1,c}$.

III. MEASUREMENTS OF ACOUSTICAL PRESSURE PHASORS

Many thermoacoustic quantities in the engine, such as pressure drops, acoustic power output, heat flows, and streaming mass fluxes, typically scale as the square of the ratio of the acoustic pressure to mean pressure. Often these quantities also depend on the temperature ratio across the regenerator. To separate the dependencies, the pressure ratio is held constant by adjusting \dot{Q}_h while T_h is varied by adjusting the variable acoustic load. Therefore, we must pick a reference location where the pressure amplitude will be held constant. We choose the pressure $p_{ref} = |p_{1,ref}|$ immediately above the main cold heat exchanger [see Figs. 1(b) and 2(b)] as it determines \dot{W}_c and therefore the acoustic power output and heat flow into the engine. Therefore, all acoustic amplitudes will be quoted in terms of p_{ref}/p_m .

Analysis of the engine begins with the acoustics within the torus section. In addition to the pressure amplitude, the important quantities are the magnitude and phase of the volumetric velocity at the hot and cold ends of the regenerator. Although these quantities are not directly measurable, related quantities such as the pressure drop across the regenerator and jet pump are readily measured. Since U_1 and the local resistance depend on location in the regenerator, the regenerator pressure drop $\Delta p_{1,regen}$ comes from a weighted average of U_1 within the regenerator. Since the jet pump has negligible compliance, U_1 is constant there, and the pressure drop across the jet pump is determined by $U_{1,c}$.

We will compare the pressure-drop data to the results of two different models, the impedance model of Fig. 2(b) and a more exact DeltaE model.^{27,28} The DeltaE model is based on the as-built dimensions of the engine, and it also includes ‘‘minor losses’’ where the flow expands in a diffuser, turns in an elbow, jets from an orifice, or merges with another flow. The dissipation associated with these minor losses is based on steady-flow correlations,¹⁹ and will be discussed further in the later section on the jet pump. The term ‘‘minor loss’’ originates in the analysis of (long) piping systems where entry effects, valve constrictions, bends, etc., are ‘‘minor’’ compared to the energy loss due to flow through long, straight piping sections (e.g., Ref. 29). In devices such as the engine described here, these minor losses have significant consequences.

Starting with the impedance model of Fig. 2(b), the pressure drop across the jet pump plus regenerator is given by $\Delta p_{1,jp+regen} = R_{jp} U_{1,c} + \Delta p_{1,regen}$. Substituting Eqs. (11) and (13) we find

$$\frac{\Delta p_{1,jp+regen}}{p_{1,c}} = \omega^2 LC \frac{(1 + gR_0 C_0 / 2R_{St} C)(1 - iR_{fb}/\omega L)}{1 + (i\omega L/R_{St})(1 - iR_{fb}/\omega L)}. \quad (14)$$

Before making a comparison, we make several simplifications. In the low-amplitude limit, $R_{fb} \ll \omega L$ because the radius of the inertance is much larger than a viscous or thermal penetration depth. At high acoustic amplitudes, R_{fb} increases due to minor losses and turbulent flow,³⁰ but the gentle transitions in the feedback flow path keep $R_{fb} \leq 0.1\omega L$ even at $p_{ref}/p_m = 0.10$. Therefore, we will ignore $R_{fb}/\omega L$ terms in Eq. (14) since they contribute very little to the magnitude and only a few degrees of phase to the right hand side of Eq. (14). However, if a particular design results in $R_{fb} \approx \omega L$, these terms (especially the one in the numerator) cannot be ignored. The low-amplitude limit also allows us to take $R_{St} \approx R_0(\tau + 1)f/2$, ignoring R_{jp} . This is not such a good approximation at $p_{ref}/p_m = 0.10$, where $R_{jp} \approx R_0(\tau + 1)f/2$. Using these approximations, Eq. (14) becomes

$$\frac{\Delta p_{1,jp+regen}}{p_{1,c}} = \omega^2 LC \frac{1 + gC_0/fC(\tau + 1)}{1 + 2i\omega L/fR_0(\tau + 1)}. \quad (15)$$

Finally, we note that the volume of the inertance must be included when calculating C as it contributes a significant compliance.

The lower and upper crosses in Fig. 3 are the result of Eq. (15) with $\tau = 2$ and 3, respectively. The filled symbols are the measured $\Delta p_{1,jp+regen}/p_{1,c}$ at p_{ref}/p_m ranging from 0.026 to 0.10 with the acoustic amplitude higher for the data nearer the real axis. All data are taken with $\tau \approx 3$ except for $p_{ref}/p_m = 0.026$ which is taken at $\tau \approx 2$. Over this range of amplitudes, the agreement between the detailed impedance model of Fig. 2(b) and the measured data is excellent; better than 10% in magnitude and a few degrees in phase. The open symbols are $\Delta p_{1,jp+regen}/p_{1,c}$ calculated using DeltaE. The numerical model, which is more accurate in computing the effective values of L and C in the feedback inertance and includes dissipation due to turbulence and minor losses, shows even better agreement.

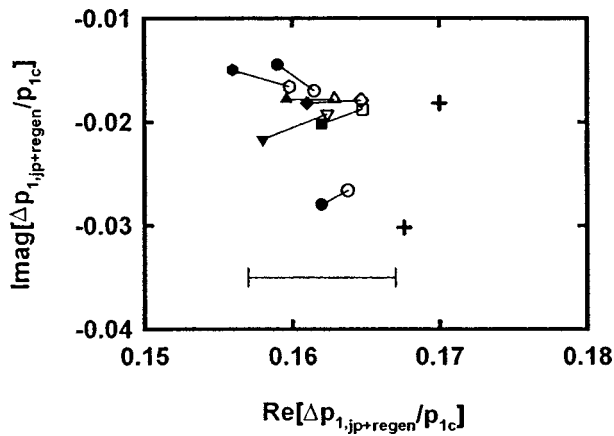


FIG. 3. Real and imaginary components of $\Delta p_{1,jp+regen}/p_{1,c}$, the pressure drop across the jet pump plus regenerator normalized by the acoustic amplitude. The upper cross is the result of the impedance model of Fig. 2(b) given in Eq. (15) with $\tau=3$. The lower cross is calculated with $\tau=2$. The filled symbols are the measured values of $\Delta p_{1,jp+regen}/p_{1,c}$ at $p_{ref}/p_m = 0.026, 0.038, 0.051, 0.061, 0.069, 0.088,$ and 0.10 with larger amplitudes nearer the top of the figure. All measurements are taken with $\tau \approx 3$ except for $p_{ref}/p_m = 0.026$ which is taken at $\tau \approx 2$. This low-amplitude measurement should be compared with the lower cross. The open symbols are calculated with DeltaE using the same value of τ as the experimental data. At each amplitude, the experimental data and DeltaE result are connected with a line to ease the comparison. Over this span of amplitudes, there is good agreement between the measured values and the impedance model indicating the approximations used in deriving Eq. (15) are valid. The DeltaE model, which is more accurate in computing L and C and takes into account the nonlinear resistances of the feedback inertance and jet pump due to minor losses and turbulence, shows even better agreement as the amplitude is varied. The error bar near the bottom of the figure shows the worst-case uncertainty in the real part of the measured $\Delta p_{1,jp+regen}/p_{1,c}$. The uncertainty in the real part is mostly due to changes in the pressure sensors' sensitivity caused by thermal drifts. The uncertainty in the imaginary part is negligible on this scale.

Even though the approximations used in reaching Eq. (15) are far from being valid at $p_{ref}/p_m = 0.10$, the agreement in Fig. 3 is still quite good. The explanation of this robustness is similar to the discussion that follows Eq. (13). Since $\omega L \ll R_0(\tau+1)f/2$ and the feedback inertance has been designed so that $R_{fb} \ll \omega L$ even at high amplitude, $\Delta p_{1,jp+regen}$ is mostly determined by L and C . Errors in the impedance of the regenerator and jet pump do not have a large effect. If the terms in Eq. (15) other than $\omega^2 LC$ are ignored, $\Delta p_{1,jp+regen}/p_{1,c} = 0.166$, which differs from the measured $\Delta p_{1,jp+regen}/p_{1,c}$ by less than 5% in magnitude and 10° in phase. Ignoring the nonideal properties of the acoustic elements in the torus, such as viscous flow resistance, thermal relaxation losses, and minor losses, does not lead to large errors in $\Delta p_{1,jp+regen}$. Therefore, the approximate expressions for the minor losses used in the DeltaE model, which are discussed in the section on Gedeon streaming, are expected to result in better agreement between the measurement and calculations, but errors in these approximations will not effect the results significantly.

As a check of how well the properties of the jet pump and regenerator are known, Fig. 4 presents the pressure drops across these individual elements as a function of acoustic amplitude and T_h . The filled and open symbols are measured values of $\Delta p_{1,regen}$ and $\Delta p_{1,jp}$, respectively. The two data points for each acoustic amplitude are taken at the high and

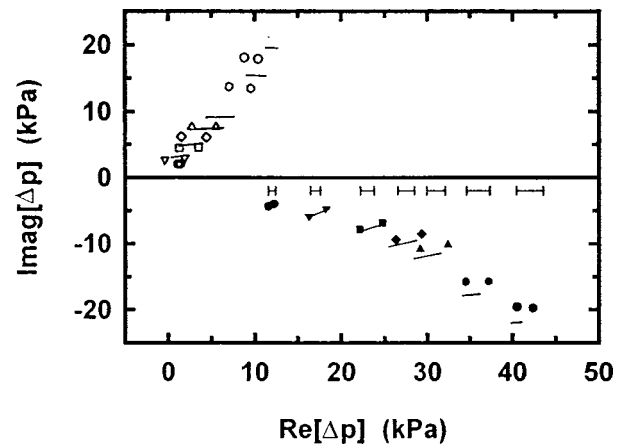


FIG. 4. Real and imaginary parts of $\Delta p_{1,jp}$ (open symbols) and $\Delta p_{1,regen}$ (filled symbols) measured at the same values of p_{ref}/p_m as shown in Fig. 3. The two symbols at each amplitude represent the upper and lower extremes of T_h . The upper limit is typically 700°C while the lower limit is amplitude dependent. The solid lines are DeltaE calculations at the same amplitudes and between the same temperature extremes. The error bars near the middle of the figure indicate the typical uncertainty in the real part of the $\Delta p_{1,regen}$ measurements. Each individual error bar applies to the two equal-amplitude data points directly below the error bar and to the real part of the corresponding $\Delta p_{1,jp}$ data points in the upper half of the figure. The uncertainty in the imaginary parts of $\Delta p_{1,jp}$ and $\Delta p_{1,regen}$ is negligible on this scale.

low extremes of T_h . The solid lines are calculated with DeltaE between the same values of T_h . The only adjustable parameter used in this part of the model is the relative surface roughness ϵ of the piping used in the feedback inertance.²⁹ The DeltaE results in Fig. 4 are generated with $\epsilon = 1.8 \times 10^{-3}$ corresponding to an absolute roughness of $140 \mu\text{m}$. This absolute roughness is consistent with what we have used in DeltaE models to obtain agreement with measurements in other thermoacoustic devices. Increasing or decreasing the surface roughness used in the calculation by a factor of 2 does not effect the pressure-drop predictions significantly. The agreement here is quite good, indicating that the acoustical phenomena in the torus section are well understood. In particular, the agreement between measured and calculated $\Delta p_{1,jp}$ provides evidence that the model used for the minor loss acoustic resistance given in Eq. (24) is reasonably accurate. If the acoustic resistance predicted by this model were ignored, the predicted magnitude of the jet-pump impedance would be approximately 3.3 times smaller at $p_{ref}/p_m = 0.10$.

With confidence in the DeltaE model, it is used to calculate the volumetric-velocity phasors in the regenerator at $\tau = 3.3$. In Table I, the results of the DeltaE calculations are compared with those of the detailed impedance model of Fig. 2(b) performed in two ways, setting $R_{fb} = 0$ or $R_{fb} = R_{jp} = 0$. When R_{jp} is taken into account, there is reasonable agreement in $|U_{1,c}|$ and $|U_{1,h}|$ between DeltaE and the detailed impedance model. If R_{jp} is ignored at high amplitude where $R_{jp} \approx f(\tau+1)R_0/2$, there are large errors in the magnitudes due to the $\omega^2 LC/R_{st}$ term in Eq. (13). However, in neither case do the impedance model calculations reproduce the phase of $U_{1,c}$ or $U_{1,h}$. Much of this phase error can be attributed to the open spaces between the jet pump and regenerator which contribute additional compliances not included

TABLE I. Calculated values of acoustic admittances $U_{1,c}/p_{1,c}$ and $U_{1,h}/p_{1,c}$ at $p_{\text{ref}}/p_m=0.026$ and 0.10 with $\tau=3.3$ using three different methods: DeltaE, the impedance model of Fig. 2(b) with $R_{\text{fb}}=0$, and the impedance model of Fig. 2(b) with $R_{\text{fb}}=R_{\text{jp}}=0$. The values of U_1/p_1 are given in $\text{m}^3/\text{Pa s}$. At low amplitude, $R_{\text{jp}} \ll (\tau + 1)fR_0/2$ and $R_{\text{fb}} \ll \omega L$. Therefore, all three methods are in reasonable agreement at $p_{\text{ref}}/p_m=0.026$. At $p_{\text{ref}}/p_m=0.10$, $R_{\text{jp}} \approx (\tau + 1)fR_0/2$ and ignoring R_{jp} leads to significant error in the magnitudes of $U_{1,c}$ and $U_{1,h}$. There are phase errors of $\approx 15^\circ - 30^\circ$ in the impedance model, much of which is due to ignoring compliances of components between the jet pump and regenerator.

p_{ref}/p_m		DeltaE		$R_{\text{fb}}=0$		$R_{\text{fb}}=R_{\text{jp}}=0$	
0.026	$U_{1,c}/p_{1,c}$	5.0×10^{-8}	30°	5.5×10^{-8}	16°	5.8×10^{-8}	15°
0.026	$U_{1,h}/p_{1,c}$	1.5×10^{-7}	-30°	1.8×10^{-7}	-14°	1.9×10^{-7}	-13°
0.100	$U_{1,c}/p_{1,c}$	3.5×10^{-8}	46°	3.8×10^{-8}	17°	5.8×10^{-8}	15°
0.100	$U_{1,h}/p_{1,c}$	9.6×10^{-8}	-45°	1.3×10^{-7}	-25°	1.9×10^{-7}	-13°

in the impedance model. Although the impedance model does not predict the phases of $U_{1,c}$ or $U_{1,h}$ with great accuracy, we believe it is useful for making estimates in the initial design of an engine. Also, the intuitive picture it provides is indispensable when optimizing the engine dimensions while performing more precise, numerical calculations such as with DeltaE.

IV. STREAMING HEAT TRANSPORT AND ITS SUPPRESSION

We now discuss two types of streaming that occur within the engine, their effect on the engine, and methods of suppression.

A. Gedeon streaming

Gedeon streaming—acoustic streaming around the torus—is a major problem to be overcome.²⁰ Gedeon⁷ has discussed how a second-order, time-averaged mass flux \dot{M}_2 can exist in Stirling systems which contain a closed-loop path. The acoustic network of the torus in Fig. 1(b) clearly provides such a path. Gedeon argues that \dot{M}_2 is given by

$$\dot{M}_2 = \text{Re}[\rho_1 \tilde{U}_1]/2 + \rho_m U_{2,0}, \quad (16)$$

where $U_{2,0}$, the second-order time-independent volumetric velocity, is the next term in the expansion given in Eq. (1). Since $\rho_1 \propto p_1$, the first term on the right hand side of Eq. (16) is nonzero wherever the acoustic power flux is nonzero, such as around the torus of Fig. 1(b). If no measures are taken to impose a $U_{2,0}$ to cancel the first term, the resulting mass flux convects heat away from the hot heat exchanger and deposits it at the secondary cold heat exchanger, creating an unwanted heat leak of $\dot{Q}_{\text{leak}} = \dot{M}_2 c_p (T_h - T_c)$. Here, c_p is the constant-pressure heat capacity of the helium. At the cold end of the regenerator, the first term on the right hand side of Eq. (16) can be rewritten $\text{Re}[\rho_1 \tilde{U}_1]/2 = \rho_{m,c} \dot{W}_c / p_m$ where $\rho_{m,c}$ is the mean density evaluated at T_c and T_1 is assumed to be zero. Using this result and Eq. (5), \dot{Q}_{leak} can be rewritten

$$\frac{\dot{Q}_{\text{leak}}}{\dot{W}_{\text{junc}}} = \frac{\rho_{m,c} c_p T_c}{p_m} = \frac{\gamma}{\gamma - 1} \quad (17)$$

if $U_{2,0}=0$. For a monatomic ideal gas, this ratio is 2.5. The scale of this heat leak can be understood by considering a reversible engine operating with $T_h \rightarrow \infty$, and therefore having Carnot efficiency¹⁴ $\eta_C \rightarrow 1$. The heat leak of Eq. (17)

would reduce the maximum possible efficiency to 0.29. Therefore, this streaming mechanism is a considerable load on the hot heat exchanger and must be suppressed.

To enforce $\dot{M}_2=0$, a nonzero $U_{2,0}$ must flow around the feedback loop and up through the regenerator. The only significant steady-flow resistance in this path is the regenerator. Swift *et al.*²⁰ have shown that the pressure drop across the regenerator that is needed to drive the correct $U_{2,0}$ in the low-Reynolds-number limit is given by

$$\Delta p_{2,0} \approx \frac{6}{S r_h^2 p_m} \int_{\text{reg}} \mu_m(x) \dot{W}(x) dx, \quad (18)$$

where $\mu_m(x)$ and $\dot{W}(x)$ are the spatially dependent coefficient of viscosity and acoustic power flow in the regenerator. Assuming a constant temperature gradient throughout the regenerator (only valid when the streaming is suppressed) and $\dot{W}(x) = \dot{W}_c T_m(x)/T_c$, the integral in Eq. (18) yields

$$\Delta p_{2,0} = \frac{6 \mu_c l}{(b+2) S r_h^2 p_m} \left[\frac{\tau^{b+2} - 1}{\tau - 1} \right] \dot{W}_c \approx \frac{R_0(\tau+1)f}{2} \frac{\dot{W}_c}{p_m}. \quad (19)$$

This required pressure drop is typically in the range 300–1500 Pa, with the higher pressure on the hot side of the regenerator.

One way²⁰ to impose such a $\Delta p_{2,0}$ across the regenerator is to use the asymmetry of hydrodynamic end effects. When high-Reynolds-number flow makes an abrupt transition from a pipe of small cross-sectional area to a larger area, the transition is accompanied by jet flow and turbulence,³⁰ Bernoulli's equation is not expected to hold, and the transition generates an additional pressure drop and dissipation. This phenomenon is often referred to as ‘‘minor loss.’’ The additional pressure drop Δp_{ml} is

$$\Delta p_{\text{ml}} = K \rho v^2/2, \quad (20)$$

where K depends on the flow geometry and is termed the ‘‘minor loss coefficient.’’ For an abrupt transition where steady flow *expands* into a much larger cross-sectional area, $K = K_{\text{exp}} \approx 1$.^{19,30,29} The value of K_{exp} is approximately constant and independent of the geometry of the transition. For steady flow in the opposite direction, *contracting* into the smaller pipe, $K = K_{\text{con}}$ is strongly dependent on geometrical details. If the edge of the entrance is sharp, $K_{\text{con}} \approx 0.5$. As the edge of the entrance is rounded, K_{con} falls until the radius of the rounding, r , is such that $r/D \geq 0.15$.^{19,30,29} Here, D is the

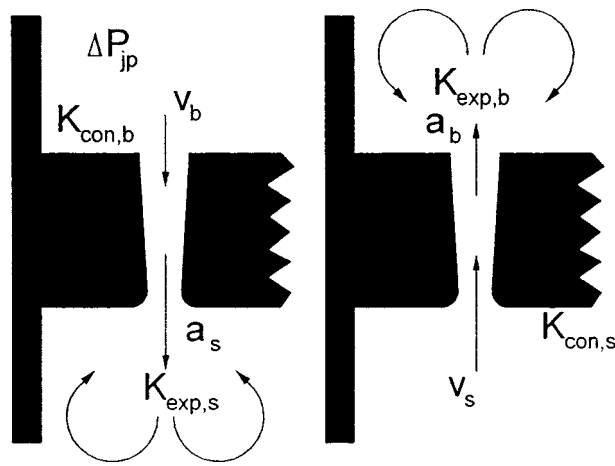


FIG. 5. Schematic diagram of the jet pump. The actual jet pump has two adjustable slots, only one of which is shown here. It is shown for both directions of flow. Areas a_s and a_b refer to total areas (both slots). The big opening has area $a_b = 3 \text{ cm}^2$ and the small opening area a_s is adjustable, from outside the pressure vessel, over the range $0\text{--}3 \text{ cm}^2$. Subscripts s and b refer to the small and big openings, respectively. The two flow patterns represent the first-order acoustic velocity during the two halves of the acoustic cycle. Approximate values for the minor loss coefficients are $K_{\text{exp},b} = K_{\text{exp},s} = 1.0$, $K_{\text{con},b} = 0.5$, and $K_{\text{con},s} = 0.04$. The time-averaged pressure drop $\overline{\Delta p_{\text{jp}}}$ is generated such that the pressure is higher above the jet pump.

diameter of a circular opening which forms the entrance. At these values of r , $K_{\text{con}} \approx 0.04$ and the flow resistance of an abrupt transition displays a nearly perfect asymmetry with respect to flow direction.

Figure 5 shows a schematic of the “jet pump” which is located between the compliance and main cold heat exchanger in Fig. 1(b). The two different flow patterns shown represent the first-order acoustic velocity during the two halves of the acoustic cycle. The jet pump utilizes minor losses by channeling the flow above the main cold heat exchanger through two parallel tapered rectangular channels that open abruptly into the larger space below the jet pump. The long dimension (into the page) of the outlets is fixed at 51 mm . The short dimension is adjustable and typically set near $\delta g = 1\text{--}2 \text{ mm}$. The edges of the outlets are rounded with a 0.8-mm radius, which is estimated to be enough to reduce $K_{\text{con},s}$ to nearly zero. The subscripts s and b correspond to the small and big openings at opposite ends of the jet pump. If the channels leading up to the expansion were not tapered, nearly the same minor loss would take place at both ends and the jet pump would show little asymmetry. The taper increases the cross-sectional area at the large end thereby decreasing the velocity. From Eq. (20), the reduction in velocity results in a much smaller pressure drop.

To estimate the time-averaged pressure drop across the jet pump, the coefficients K_{exp} and K_{con} are assumed to have the same values in oscillating flow as they do in steady flow. The accuracy of this assumption is unknown, although the large displacement amplitudes ($|x_1|/\delta g \approx 200$) give us hope that at each instant of time, the flow has little memory of its time dependence. Taking the instantaneous velocities to be $v_s(t) = v_{1,s} \sin \omega t$ and $v_b(t) = (a_s/a_b)v_s(t)$ with positive velocities downward, the instantaneous pressure drop due to the first-order velocity is given by

$$\Delta p_{\text{jp}}(0 \leq t \leq \pi/\omega) = \frac{\rho_m}{2} (K_{\text{con},b} v_b^2 + K_{\text{exp},s} v_s^2), \quad (21)$$

$$\Delta p_{\text{jp}}(\pi/\omega \leq t \leq 2\pi/\omega) = -\frac{\rho_m}{2} (K_{\text{exp},b} v_b^2 + K_{\text{con},s} v_s^2).$$

Again, we assume that the coefficients K_{exp} and K_{con} have the same values in oscillatory flow as they do in steady flow, and that Eq. (20) can be applied instantaneously throughout the acoustic cycle. The time-averaged pressure drop across the jet pump is found to be

$$\overline{\Delta p_{\text{jp}}} = \frac{\rho_m |U_{1,\text{jp}}|^2}{8a_s^2} \left[(K_{\text{exp},s} - K_{\text{con},s}) + \left(\frac{a_s}{a_b} \right)^2 (K_{\text{con},b} - K_{\text{exp},b}) \right], \quad (22)$$

where $U_{1,\text{jp}}$ is the amplitude of the first-order volumetric velocity through the jet pump. For the orientation of the jet pump in Fig. 1(b), Δp_{jp} has the correct sign to suppress the streaming around the feedback loop.²⁰ In this derivation, we have ignored the pressure drop due to the inertance and linear resistance of the jet pump as they do not contribute to $\overline{\Delta p_{\text{jp}}}$.

In addition to generating $\overline{\Delta p_{\text{jp}}}$, the jet pump also dissipates acoustic power.²⁰ The instantaneous power dissipation is given by $\Delta p_{\text{jp}}(t)U_{\text{jp}}(t)$. Averaging over one acoustic cycle, the time-averaged power dissipation is

$$\dot{E} = \frac{\rho_m |U_{1,\text{jp}}|^3}{3\pi a_s^2} \left[(K_{\text{exp},s} + K_{\text{con},s}) + \left(\frac{a_s}{a_b} \right)^2 (K_{\text{con},b} + K_{\text{exp},b}) \right]. \quad (23)$$

For a pure acoustic resistance R , the time-averaged power dissipation is given by $\dot{E} = R|U_1|^2/2$. Using this relation, we can assign a resistance to the jet pump of

$$R_{\text{jp}} = \frac{2\rho_m |U_{1,\text{jp}}|}{3\pi a_s^2} \left[(K_{\text{exp},s} + K_{\text{con},s}) + \left(\frac{a_s}{a_b} \right)^2 (K_{\text{con},b} + K_{\text{exp},b}) \right]. \quad (24)$$

This resistance is in addition to that due to viscous and thermal relaxation losses. The minor loss resistance of other elements in the engine is calculated in a similar way.

Figure 6(a) and (b) demonstrate the effectiveness of the jet pump. Figure 6(b) shows the time-dependent $\Delta p_{\text{jp}}(t)$, measured using a differential piezoresistive pressure sensor,²² displayed as a function of the time phase $\phi(t)$ of the acoustic cycle. The sensor itself is located outside the pressure vessel, and approximately 10 cm of 1.5-mm -diameter copper tubing is used to connect the front and back of the sensing membrane to the top and bottom of the jet pump. The ends of the copper tubing are located close to the corners formed by the plate that houses the jet pump and the pressure-vessel wall. We believe these locations are best because they are nearly stagnation zones of the secondary flows generated by the jet pump, but we have not investigated how

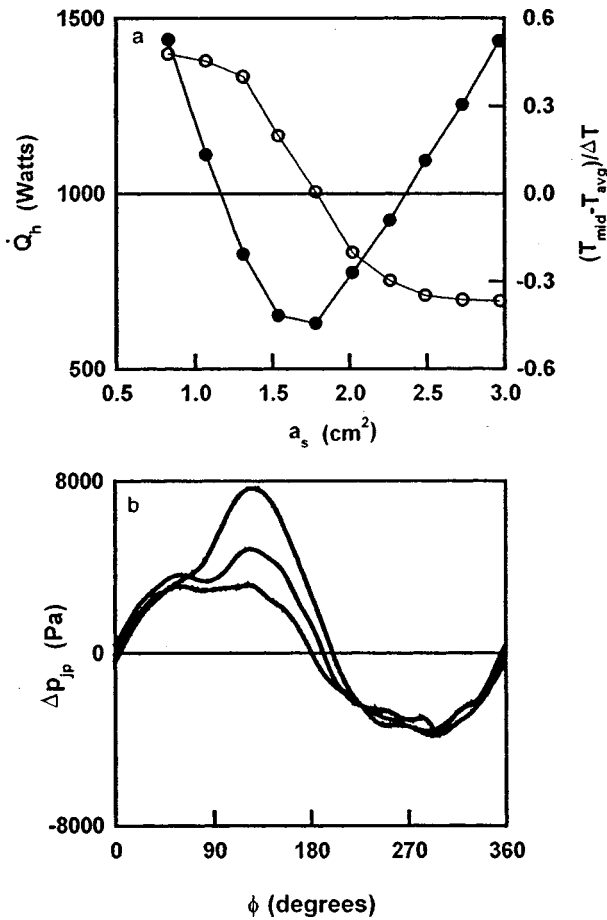


FIG. 6. (a) \dot{Q}_h (filled symbols) and $(T_{mid} - T_{avg})/\Delta T$ (open symbols) vs the jet area a_s . Here, $\Delta T = T_h - T_c$ and $T_{avg} = (T_h + T_c)/2$. As a_s is varied, \dot{Q}_h is adjusted to maintain $p_{ref}/p_m = 0.036$, and hence $Re[\rho_1 \bar{U}_1]$ nearly constant within the regenerator. With $a_s = 1.8$ cm², $T_{mid} = T_{avg}$ indicating that \dot{M}_2 is completely suppressed. With $\dot{M}_2 = 0$, $\dot{Q}_{leak} = 0$ and the heat input \dot{Q}_h needed to maintain the oscillations is at a minimum. Typical uncertainties are ± 20 W in \dot{Q}_h , ± 0.04 cm² in a_s , and $\pm 1\%$ in $(T_{mid} - T_{avg})/\Delta T$. (b) Measurements of $\Delta p_{jp}(t)$ as a function of the time phase of the acoustic cycle $\phi(t)$. The lowest curve (at $\phi = 120^\circ$), obtained with $a_s = 3.0$ cm², has $\overline{\Delta p_{jp}} = 120$ Pa; the middle curve, obtained with $a_s = 1.8$ cm², has $\overline{\Delta p_{jp}} = 630$ Pa; the highest curve, obtained with $a_s = 0.8$ cm², has $\overline{\Delta p_{jp}} = 1160$ Pa. The middle setting suppresses \dot{M}_2 , as shown in (a). The sinusoidal background pressure drop is due to the inertance and linear resistance of the jet pump.

accurately this technique determines Δp_{jp} . Therefore, the magnitudes of Δp_{jp} cannot be trusted, but changes in Δp_{jp} between different settings of a_s allow a qualitative measure of the action of the jet pump.

The lowest curve (at $\phi = 120^\circ$) in Fig. 6(b) displays $\Delta p_{jp}(t)$ with $a_s = a_b = 3.0$ cm². Time averaged, this curve does not yield a significant $\overline{\Delta p_{jp}}$, so a large \dot{M}_2 flows down through the regenerator and TBT causing a large \dot{Q}_{leak} . To maintain the oscillation at $p_{ref}/p_m = 0.036$, Fig. 6(a) shows that nearly 1500 W of \dot{Q}_h is necessary, with more than half of this \dot{Q}_h carried away by \dot{M}_2 . Also, the temperature T_{mid} at the axial midpoint of the regenerator is held significantly below its expected temperature $T_{avg} = (T_h + T_c)/2$ due to the flux of cold gas entering the cold end of the regenerator. The middle curve in Fig. 6(b) corresponds to $a_s = 1.8$ cm² in Fig.

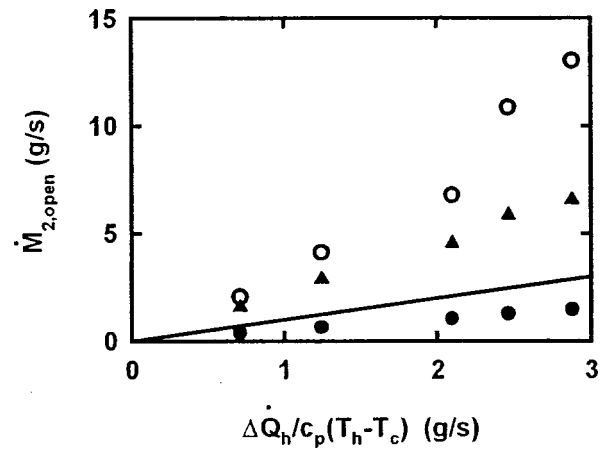


FIG. 7. Estimates of the Gedeon streaming mass flux $\dot{M}_{2,open}$. The solid line has slope 1 and represents $\Delta \dot{Q}_h / c_p (T_h - T_c)$. The filled circles are $\rho_{m,c} \bar{W}_c / p_m$. The filled triangles and open circles are the result of estimating $\dot{M}_{2,open}$ from the measured and calculated values of $\overline{\Delta p_{jp,0}}$, respectively.

6(a). The resulting $\overline{\Delta p_{jp}}$ generated by the jet pump enforces $\dot{M}_2 = 0$, so that $T_{mid} = T_{avg}$ and \dot{Q}_{leak} is eliminated. Therefore, \dot{Q}_h needed to maintain $p_{ref}/p_m = 0.036$ is at its minimum of 630 W. The highest curve in Fig. 6(b) corresponds to $a_s = 0.8$ cm² in Fig. 6(a). The resulting Δp_{jp} exceeds the required $\Delta p_{2,0}$, so $\dot{M}_2 < 0$, implying that the time-averaged mass flux flows up through the TBT and regenerator. With $\dot{Q}_h \approx 1500$ W, the convective heat leak has returned, and $T_{mid} > T_{avg}$ due to the hot gas entering the hot end of the regenerator. These data demonstrate that \dot{M}_2 causes a significant and unwanted heat load that can be completely eliminated by Δp_{jp} , and that T_{mid} can be used to indicate when $\dot{M}_2 = 0$. Also, the broad minimum in \dot{Q}_h in Fig. 6(a) shows that the cancellation of \dot{M}_2 is insensitive to small variations in a_s .

The experiment described above demonstrates that the jet pump can stop the Gedeon streaming mass flux. A different experiment is used to determine the magnitude of the mass flux so it can be compared with several equations in this section. To avoid confusion, the streaming mass flux with a_s at its fully open position of 3 cm² is referred to as $\dot{M}_{2,open}$. At several fixed values of p_{ref}/p_m , two measurements of \dot{Q}_h are performed; one with a_s adjusted so that $\dot{M}_2 = 0$ and a second with a_s fully open, i.e., $a_s = 3.0$ cm². With a_s fully open, nearly all of the extra heat input $\Delta \dot{Q}_h$ is carried away by $\dot{M}_{2,open}$ which is calculated as $\dot{M}_{2,open} = \Delta \dot{Q}_h / c_p (T_h - T_c)$. If $U_{2,0} = 0$ when $a_s = 3.0$ cm², Eq. (16) shows that $\dot{M}_{2,open} = \rho_{m,c} \bar{W}_c / p_m$. Using the DeltaE model developed in the previous section to compute \bar{W}_c , the measured $\dot{M}_{2,open}$ and $\rho_{m,c} \bar{W}_c / p_m$ are compared. The horizontal axis in Fig. 7 is given by the measured values of $\Delta \dot{Q}_h / c_p (T_h - T_c)$. The solid line has slope 1 and represents $\dot{M}_{2,open} = \Delta \dot{Q}_h / c_p (T_h - T_c)$. The filled circles are $\dot{M}_{2,open} = \rho_{m,c} \bar{W}_c / p_m$ and are roughly a factor of 2 lower than $\Delta \dot{Q}_h / c_p (T_h - T_c)$. We believe that the combined uncertainty in the $\Delta \dot{Q}_h$ measurement of $\dot{M}_{2,open}$ and the computation of

\dot{W}_c cannot account for this difference. This result suggests that there are additional sources of $\Delta p_{2,0}$ in the torus, probably at locations of high velocity with asymmetry in minor loss coefficients, which cause nonzero $U_{2,0}$ even when a_s is fully open. The velocity in the secondary cold heat exchanger is high enough to generate a significant $\Delta p_{2,0}$, but we believe there is very little asymmetry in its minor losses. The resonator junction, on the other hand, has both large velocities and significantly asymmetric minor losses. When $\Delta \dot{Q}_h/c_p(T_h - T_c) = 2.9$ g/s, we estimate that the resonator junction generates $\Delta p_{2,0} \approx 900$ Pa, which would drive roughly $\rho_m U_{2,0} = 2.8$ g/s in the same direction as $\rho_{m,c} \dot{W}_c/p_m$. This would more than account for the 1.4 g/s difference between $\rho_{m,c} \dot{W}_c/p_m$ and $\dot{M}_{2, \text{open}}$ obtained from $\Delta \dot{Q}_h$. Given the uncertainty in the use of steady-flow minor loss correlations for oscillating flow, it seems likely that the resonator junction is responsible for the additional $\dot{M}_{2, \text{open}}$.

Next, the values of $\dot{M}_{2, \text{open}}$ obtained from $\Delta \dot{Q}_h$ are compared with those inferred from $\Delta p_{\text{jp},0}$, the time-averaged pressure drop required to force $\dot{M}_2 = 0$. Rewriting Eq. (19) in terms of $\dot{M}_{2, \text{open}}$, we find $\dot{M}_{2, \text{open}} = [2\rho_m/R_0(\tau + 1)f]\Delta p_{\text{jp},0}$. If the measured values of $\Delta p_{\text{jp},0}$ are used in this expression, the result is the filled triangles in Fig. 7. Alternately, Eq. (22) and a DeltaE estimate of $U_{1,\text{jp}}$ can be used to calculate the expected $\Delta p_{\text{jp},0}$ which is then used to estimate $\dot{M}_{2, \text{open}}$. This result is shown as the open circles in Fig. 7. The discrepancy between the open circles and the filled triangles may be due to systematic errors in the measurement of Δp_{jp} or may be due to our imperfect knowledge of minor loss coefficients in oscillating flow. The cause of the even larger discrepancy between these estimates of $\dot{M}_{2, \text{open}}$ and the solid line is unknown and a subject of future research. At $\Delta \dot{Q}_h/c_p(T_h - T_c) = 2.9$ g/s, the $\dot{M}_{2, \text{open}}$ obtained from the calculated $\Delta p_{\text{jp},0}$ is 4.5 times higher than $\Delta \dot{Q}_h/c_p(T_h - T_c)$, roughly consistent with observations made by Swift *et al.*²⁰ in a similar device.

To summarize, when no measures are taken to suppress Gedeon streaming, the magnitude of $\dot{M}_2 = \dot{M}_{2, \text{open}}$ is due to $\rho_{m,c} \dot{W}_c/p_m$ and other generators of $\Delta p_{2,0}$ within the torus. When these are taken into account, we find rough agreement between the calculated $\dot{M}_{2, \text{open}}$ and $\dot{M}_{2, \text{open}}$ measured from $\Delta \dot{Q}_h$. More precise comparisons are not possible due to a lack of experimental data on minor loss coefficients in oscillating flow. If $\rho_{m,c} \dot{W}_c/p_m$ or the measured $\dot{M}_{2, \text{open}}$ is used to estimate $\Delta p_{\text{jp},0}$, we find large, unexplained discrepancies with Eq. (22).

B. Rayleigh (boundary-layer TBT) streaming

Olson and Swift⁸ have shown that boundary-layer driven streaming in an orifice pulse tube refrigerator's pulse tube can convect significant heat,⁸ and that an appropriately tapered pulse tube suppresses this streaming. The analogous component is the thermal buffer tube (TBT) in this engine, where we expect similar streaming effects. The streaming creates a time-averaged mass flux density about a thermal

penetration depth away from the TBT wall. Due to the viscosity of the gas, this annular sheet of mass-flux density drags the nearby gas along with it. The suppression of Gedeon streaming enforces zero total mass flux across the total cross section of the TBT. Therefore, the annular sheet of mass-flux density sets up a parabolic velocity profile across the TBT, with the gas near the center moving in the opposite direction to the gas at large radius. This flow pattern resembles an annular convection roll, and generates an unwanted heat leak by convecting heat from the hot end of the TBT to the ambient heat exchanger.

The boundary-layer analysis used in Ref. 8 should be valid if the oscillatory flow within the TBT is at low enough amplitude to be in the weakly turbulent regime, where turbulence is only generated outside the viscous and thermal boundary layers, leaving the velocity³¹ and temperature profiles within the boundary layers nearly the same as in laminar flow. As p_{ref}/p_m increases, the flow at the ambient end of the TBT moves out of the weakly turbulent regime into the transitionally turbulent regime, and approaches the fully turbulent regime, as shown in Fig. 8(a). The solid lines in Fig. 8(a) represent the values of R/δ_v and Re_D as a function of position within the TBT at the same values of p_{ref}/p_m as in Fig. 3. Here R is the local radius of the TBT and Re_D is the Reynolds number based on local peak velocity and TBT diameter. Larger values of p_{ref}/p_m are closer to the bottom of the figure. The hot end of the TBT is on the left, and the ambient end is on the right. The dashed lines indicate the boundaries between the various flow regimes. At $p_{\text{ref}}/p_m = 0.10$, much of the TBT lies within or very near the transitionally turbulent regime. The boundaries drawn between these various regimes are not sharp and were determined for incompressible flow.³¹ The acoustic flow in the TBT is compressible, so the location of the boundaries in Fig. 8(a) falls into question. Therefore, at high amplitudes, turbulence may be generated in the boundary layer, which would invalidate the analysis of Ref. 8.

After optimizing a model of the engine using DeltaE, the resulting spatial dependencies of p_1 and U_1 are used to calculate the desired local taper angle via Eq. (12) of Ref. 8. The resulting ideal shape could be CNC machined into the inside surface of the TBT. For ease of manufacture, we have instead designed a two-segment taper that closely represents this ideal shape over a broad range of p_{ref}/p_m . The upper 8.0 cm is a straight-wall cylinder with a 8.9-cm inside diameter. The lower 16.0 cm is flared with a 1.35° half-angle taper.

To study the effects of the tapered TBT, we have performed measurements with the tapered TBT and with a thin-wall stainless-steel insert that converts the tapered TBT to a straight TBT with nearly the same inside diameter as the upper 8.0 cm of tapered TBT. With the resonator as the only load on the engine, the heat delivered to the secondary cold heat exchanger is measured as a function of amplitude. We subtract away the heat loads due to radiation (discussed below), thermal conduction (discussed below), minor loss at the secondary cold heat exchanger, and boundary-layer thermoacoustic transport along the TBT walls, and assume that the remaining heat load is due to streaming within the TBT. This subtraction ranges from about 30% of the total heat load

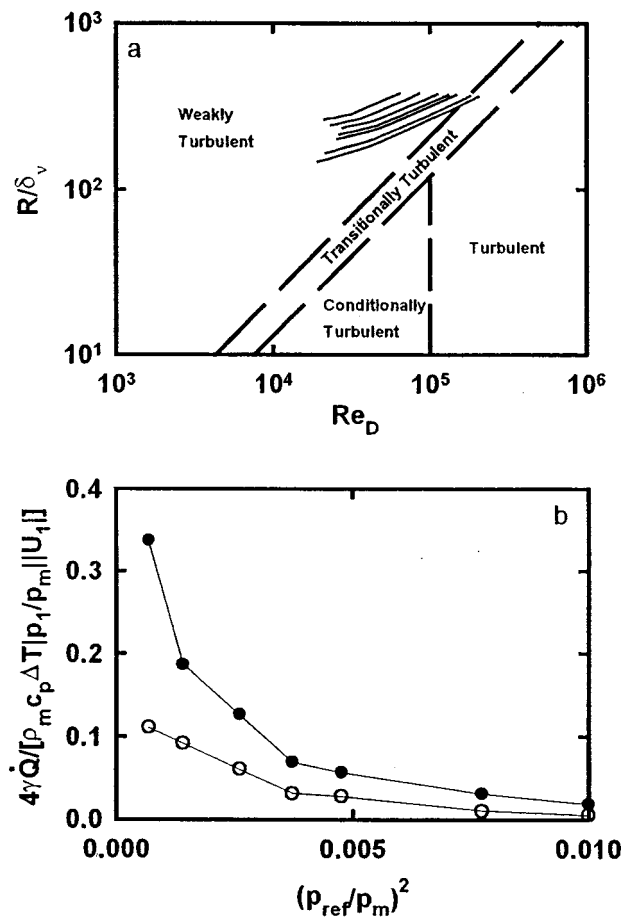


FIG. 8. (a) Flow regimes in the TBT as a function of p_{ref}/p_m and position within the TBT. The solid lines represent the values of R/δ_v and Re_D within the TBT at the same values of p_{ref}/p_m as in Fig. 3. The curves are generated using the DeltaE model developed previously. Larger values of p_{ref}/p_m are closer to the bottom of the figure. The value of T_h is different for each curve and is given by the T_h necessary to create oscillations at the corresponding p_{ref}/p_m with the resonator as the only load on the engine. The hot end of the TBT is on the left; the ambient end is on the right. The dashed lines indicate the boundaries between various oscillatory flow regimes determined for incompressible flow (Ref. 31). The transition in the flow at the boundaries is not sharp. The boundary-layer analysis in Ref. 8 is probably valid only in the weakly turbulent regime. (b) Residual heat leak, normalized by $\rho_m c_p \Delta T |p_1/p_m| |U_1| / 4\gamma$ vs $(p_{\text{ref}}/p_m)^2$. Open circles—tapered TBT; filled circles—straight TBT. Here, $\Delta T = T_{h,\text{gas}} - T_c$. p_1 varies by $\approx 1\%$ along the TBT and is taken to be the calculated p_1 at the hot end of the TBT. Both ρ_m and $|U_1|$ are taken to be the axial average of the calculated values in the TBT. Each data point is taken at the same values of p_{ref}/p_m and T_h as the corresponding curve in (a). If the boundary-layer analysis is valid, the normalized heat leak remains constant if p_1/U_1 remains constant in the TBT as the amplitude is varied. As discussed in the text, the majority of the uncertainty in the measurement of the normalized heat leak is due to thermoacoustic effects on either side of the resonator junction.

at low amplitude to 80% of the total at high amplitude. To minimize the effect of acoustic power dissipated in other parts of the engine and resonator from being conducted or thermoacoustically transported back to the secondary cold heat exchanger, six turns of water-cooled, 1/4-in. copper tubing are wrapped around each of the ducts leading to the resonator and feedback inertance. This keeps the section of duct near the resonator junction near ambient temperature even at high p_{ref}/p_m . Without this tubing, this section of duct would approach 50°C at $p_{\text{ref}}/p_m = 0.10$.

Figure 8(b) shows the results of these measurements. The open and filled circles are the normalized residual heat leak to the secondary cold heat exchanger for the tapered and straight TBT, respectively. The heat leak is normalized such that if p_1/U_1 in the TBT is constant as the amplitude is varied, the normalized heat leak would be constant and would depend only on the geometry of the TBT. This assumes that the boundary-layer analysis of Ref. 8 is valid. At the lowest amplitude, we expect a difference of 0.18 in normalized heat leak between the tapered and straight TBT based on the calculations of Ref. 8. This is roughly consistent with the measured difference of 0.23. As the amplitude increases, the difference between the straight and tapered TBTs decreases as well as the magnitude of the normalized heat leak. In absolute numbers for the tapered TBT, the residual heat leak is approximately 115 W and 36 W at $p_{\text{ref}}/p_m = 0.061$ and 0.10, respectively, when $T_{h,\text{gas}} = 725^\circ\text{C}$. This amounts to 5% and 1% of the \dot{Q}_h , respectively.

Measurements of the temperature profile along the TBT wall are consistent with the dependence of the heat leak on amplitude. At low amplitude ($p_{\text{ref}}/p_m = 0.026$), we expect the time-averaged mass-flux density at the wall to be directed downward from hot to cold, which would hold the upper half of the TBT wall near the temperature of the hot heat exchanger. In the lower half, the temperature should decrease sharply to the temperature of the secondary cold heat exchanger. This behavior is indeed observed in the tapered TBT at low amplitude. At $p_{\text{ref}}/p_m = 0.026$, the temperature at the axial midpoint of the TBT wall has decreased by only 20% of the total temperature difference spanned by the TBT. However, as the amplitude is increased, the temperature distribution becomes nearly linear with only small deviations from linearity near the ends of TBT. This indicates that the convective heat flux carried along the TBT wall is reduced.

There are several possibilities which are consistent with these observations. The first is that turbulence in the boundary layer destroys the velocity³¹ and temperature profiles responsible for the streaming, making a straight TBT equivalent to a tapered one. As more of the TBT becomes turbulent at higher amplitude, the streaming is eliminated in more of the TBT, resulting in a decreasing normalized heat leak. Alternately, the turbulence may drive radial mixing of the gas in the TBT due to changes in the velocity profile through the acoustic cycle.³¹ This radial mixing would cause heat exchange between the oppositely moving streaming flows and effectively “short out” the streaming heat load. As the amplitude increases and more of the TBT becomes turbulent, this mechanism would cause a decrease in normalized heat leak and make a straight TBT perform as well as a tapered one. Another possibility is that thermoacoustic effects on either side of the resonator junction are transporting heat into or out of the secondary cold heat exchanger. The additional heat flux would mask the effects of TBT boundary-layer streaming on the measurements, but it should not affect the temperature profile in the TBT which correlates well with the normalized heat leak. All of these explanations are merely conjectures and further research in this area is required to provide a definitive answer.

V. THERMOACOUSTIC MEASUREMENTS

With Gedeon streaming completely suppressed and Rayleigh streaming reduced to an acceptable level, we now continue with basic thermoacoustic measurements. The general approach is to move sequentially through the engine from heat input to resonator dissipation, ultimately using exergy¹⁴ to account quantitatively for all of the irreversibilities due to heat leaks and acoustic power dissipation. Some of these quantities are directly measured. Others require one step of calculation, typically using DeltaE,²⁷ after the measurement.

A. Heat leaks

Not all of the heat input \dot{Q}_h to the hot heat exchanger is delivered to the thermoacoustic processes. Some is convected away by residual streaming that is not completely suppressed. The diagnostic measurements discussed above show that these residual convective heat leaks can be reduced to an acceptable level. Additional routes for heat leaks include the metal of the regenerator screen bed, surrounding pressure-vessel wall, and TBT wall; the ceramic fiber insulation³² surrounding the TBT and regenerator; and radiation down the TBT. The heat leak caused by ordinary conduction in the helium gas is estimated to be small and is ignored in the rest of this discussion.

To determine the magnitude of these heat leaks, the engine is filled with 30-bar helium and heavily loaded with the variable acoustic load. This keeps the engine from oscillating, even at the highest operating temperature of 725 °C. Electric heat \dot{Q}_h , measured with a commercial wattmeter,¹⁸ is applied at the hot heat exchanger and returns to ambient temperature T_c at the main cold heat exchanger or secondary cold heat exchanger, or through the ceramic fiber insulation, denoted \dot{Q}_{main} , \dot{Q}_{sec} , and \dot{Q}_{ins} , respectively. The heats \dot{Q}_{main} and \dot{Q}_{sec} are determined by measuring the temperature rise and flow rate of the cooling water in the respective heat exchangers. The flow rate, which is measured with a commercial flowmeter, is restricted with a needle valve so that the temperature rise is easily measurable (5–15 °C). The heat passing through the ceramic fiber insulation is determined from the energy balance $\dot{Q}_{\text{ins}} = \dot{Q}_h - (\dot{Q}_{\text{main}} + \dot{Q}_{\text{sec}})$.

Before presenting the heat leak data, the spatial dependence of the hot temperature requires some discussion. With no acoustic oscillations present, the majority of \dot{Q}_h is carried by the TBT wall and pressure-vessel wall surrounding the regenerator, but \dot{Q}_h is injected evenly across the hot face of the regenerator. This leads to a radially outward flux of heat and a radial temperature dependence along the hot face of the regenerator. Therefore, the heat leaks along the TBT wall, regenerator pressure-vessel wall, and out through the ceramic fiber insulation are not driven by T_h , but by the temperature at the edge of the regenerator, $T_{h,\text{edge}}$ [see Fig. 1(b)]. The other major sources of heat leak, conduction along the regenerator screen and radiation down the TBT, would be determined by integrating the equation for the local heat flux over the hot face of the regenerator. This leads to an expression for the total heat flux in terms of a spatial average of the hot temperature raised to some power, e.g., $\langle T^4(r) \rangle_r$ in the case

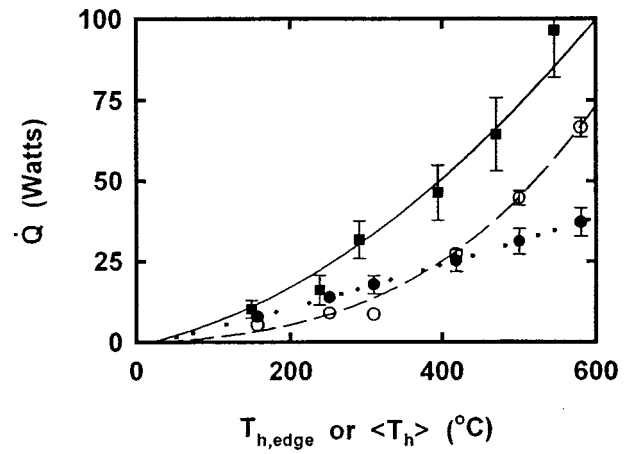


FIG. 9. Heat leaks vs $T_{h,\text{edge}}$ or $\langle T_h \rangle$. The radiation heat leak \dot{Q}_{rad} (open circles) down the TBT and the conduction heat leak \dot{Q}_{regen} (filled circles) up the regenerator screen bed are given in terms of $\langle T_h \rangle$. The heat leak \dot{Q}_{ins} (filled squares) through the ceramic fiber insulation is given in terms of $T_{h,\text{edge}}$. The dashed, dotted, and solid lines are given by Eqs. (26), (27), and (28), respectively. For the lower temperature data, the error bars are smaller than the symbols.

of radiation. For the measured T_h and $T_{h,\text{edge}}$, the difference between $\langle T^4(r) \rangle_r$ and $\langle T(r) \rangle_r^4$ is not noticeable within the experimental error. Therefore, we will quote the radiation and screen-bed-conduction heat leaks in terms of the average hot temperature $\langle T_h \rangle = \langle T(r) \rangle_r$. The conduction heat leaks along the TBT wall, regenerator pressure-vessel wall, and through the ceramic fiber insulation will be given in terms of $T_{h,\text{edge}}$. With the acoustic oscillations present, the difference between T_h and $T_{h,\text{edge}}$ is reduced due to mixing as the helium exits the hot heat exchanger and by the increased thermoacoustic heat loading.

The heat \dot{Q}_{sec} is due to radiation and metallic conduction down the TBT wall. Using the published thermal conductivity data for Inconel 625,¹⁷ which are fit by $K = K_0 + K_1 T$ (°C) with $K_0 = 9.7 \text{ W/m}^\circ\text{C}$ and $K_1 = 0.015 \text{ W/m}^\circ\text{C}^2$, the metallic conduction can be reliably calculated as

$$\dot{Q}_{\text{TBT}}(T_{h,\text{edge}}) = \frac{(T_{h,\text{edge}} - T_c)[K_0 + K_1(T_{h,\text{edge}} + T_c)/2]}{l_{\text{st}}/A_0 + l_{\text{tap}} \ln(A_f/A_0)/(A_f - A_0)}, \quad (25)$$

where l_{st} and l_{tap} are the lengths of the straight and tapered sections and A_0 and A_f are the cross-sectional areas of the TBT wall at the beginning and end of the taper. The TBT wall has a constant wall thickness for its entire length. The radiation heat leak is then extracted using $\dot{Q}_{\text{rad}}(\langle T_h \rangle) = \dot{Q}_{\text{sec}} - \dot{Q}_{\text{TBT}}(T_{h,\text{edge}})$ and is shown as the open circles in Fig. 9. The appropriate $\langle T \rangle^4$ temperature dependence is shown by \dot{Q}_{rad} , but the geometry of the hot zone is complicated and the calculation of the prefactor of $\langle T \rangle^4$ (including emissivity) would be quite involved and not very enlightening. For comparison, the dashed line is given by

$$\dot{Q}_{\text{rad}} = 0.36\sigma S(\langle T_h \rangle^4 - T_c^4), \quad (26)$$

where σ is the Stephan–Boltzman constant, S is the area of the regenerator face, and the temperatures are expressed in Kelvin. In the absence of the TBT wall, Eq. (26) represents

36% of the total energy that would be radiated into the hemisphere seen by the hot face of the regenerator.

Turning our attention to \dot{Q}_{main} , the heat leak down the pressure-vessel wall is calculated from Eq. (25) by setting $l_{\text{st}}=l$ =length of the regenerator and $l_{\text{tap}}=0$. Subtracting this from \dot{Q}_{main} leaves the heat leak down the regenerator screen bed \dot{Q}_{regen} which is given as the filled circles in Fig. 9. \dot{Q}_{regen} is expected to have a temperature dependence of the form

$$\dot{Q}_{\text{regen}}(\langle T_h \rangle) = \frac{(1-\phi)\epsilon_s S}{l} \left[K_0(\langle T_h \rangle - T_c) + \frac{K_1}{1.68} (\langle T_h \rangle^{1.68} - T_c^{1.68}) \right], \quad (27)$$

where ϵ_s is a factor which accounts for the poor thermal contact between the layers of the screen,³³ and S and ϕ are the cross-sectional area and volume porosity of the regenerator. The thermal conductivity of the 304-stainless-steel screen³⁴ which forms the bed is given by $K=K_0+K_1[T(^{\circ}\text{C})]^{0.68}$ where $K_0=13.2$ W/m $^{\circ}\text{C}$, $K_1=0.112$ W/m $^{\circ}\text{C}^{1.68}$. Using ϵ_s as an adjustable parameter, the data in Fig. 9 are best fit by $\epsilon_s=0.13$ in reasonable agreement with the current literature.³³ The fit is shown as the dotted line in Fig. 9.

Again, the difference $\dot{Q}_{\text{ins}}=\dot{Q}_h-(\dot{Q}_{\text{main}}+\dot{Q}_{\text{sec}})$ is assumed to pass through the insulation to ambient and is shown as the filled squares in Fig. 9. To calculate this heat leak, we assume linear temperature distributions along the inner surface of the insulation starting at $T_{h,\text{edge}}$ at the hot heat exchanger and decreasing in both directions to T_c at the main and secondary cold heat exchangers. Also, we consider conduction only in the radial direction. Using the published thermal conductivity data³² for the ceramic insulation packed at 12 lb/ft³, the heat leak takes the form

$$\dot{Q}_{\text{ins}}(T_{h,\text{edge}}) = \frac{\pi L_{\text{case}}(T_{h,\text{edge}}-T_c)}{\ln(R_o/R_i)} \times \left[K_0 + K_1 \frac{T_{h,\text{edge}} + 2T_c}{3} \right], \quad (28)$$

where R_i and R_o are the inner and outer radii of the insulation and L_{case} is the distance from the main cold heat exchanger to the secondary exchanger. The thermal conductivity of the insulation is fit by $K=K_0+K_1T(^{\circ}\text{C})$ with $K_0=0.014$ W/m $^{\circ}\text{C}$ and $K_1=0.17$ mW/m $^{\circ}\text{C}^2$.³² The result of Eq. (28) would fall well below the data in Fig. 9. Since the aspect ratio of the regenerator is near 1, the discrepancy is mostly likely due to axial conduction in the insulation around the regenerator. To compare the expected temperature dependence, the result of Eq. (28) is multiplied by 1.6 and plotted as the solid line in Fig. 9.

Although there are some discrepancies, the results of this section show that the overall heat leak and individual sources are reasonably well understood. The total uncertainty in the radiation and insulation heat leaks only amount to 3%–5% of \dot{Q}_h in the range $p_{\text{ref}}/p_m=0.05$ –0.10. Therefore, if both Gedeon and Rayleigh streaming are suppressed, the amount of heat entering the thermoacoustic process is well

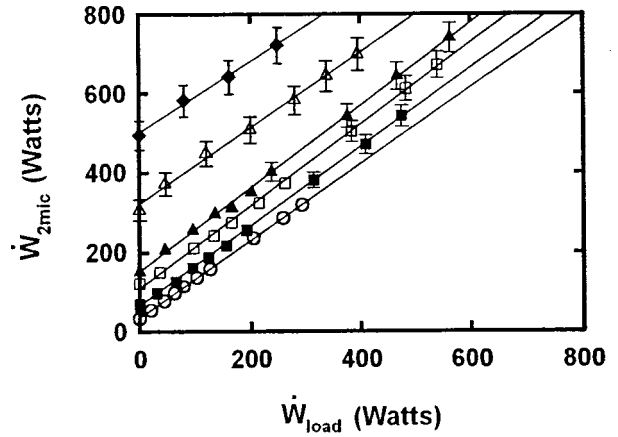


FIG. 10. $\dot{W}_{2\text{mic}}$ vs \dot{W}_{load} for the same values of p_{ref}/p_m as in Fig. 3. $p_{\text{ref}}/p_m=0.026$ has been left out for clarity. Acoustic amplitude is higher for larger values of $\dot{W}_{2\text{mic}}$. The solid lines are least-squares fits to the data. For all data except $p_{\text{ref}}/p_m=0.10$, the slopes are scattered in the range 0.96–1.05 consistent with Eq. (29). At $p_{\text{ref}}/p_m=0.10$, the slope is 0.89. This may be due to heating of the gas in the resonator causing errors in the physical parameters of the gas used in Eq. (23) of Ref. 16. The y-axis intercepts of the fits are used to extract \dot{W}_{res} and are summarized in Fig. 11. Typical uncertainties in $\dot{W}_{2\text{mic}}$ range from ± 2 W at the lowest amplitude to ± 45 W at $p_{\text{ref}}/p_m=0.10$. At smaller values of $\dot{W}_{2\text{mic}}$, the error bars are smaller than the symbols. The uncertainty in \dot{W}_{load} is $\pm 0.5\%$ and is independent of amplitude.

known. This section has emphasized heat leaks other than metallic conduction along the TBT and regenerator pressure-vessel wall, but one should not lose sight of the fact that these two sources account for over half of the total heat leak.

B. Acoustic dissipation

Analysis of acoustic dissipation begins with the resonator where direct measurements are performed. The microphones placed in the resonator in Fig. 1(a) are used to make two-microphone measurements of the acoustic power flowing past their midpoint.¹⁶ Since the resonator is a major contributor to the overall dissipation and two-microphone (two-mic) measurements can be sensitive to microphone placement, the technique is verified by comparing it with the power dissipated in the variable acoustic load \dot{W}_{load} . The load is placed at the middle port in the resonator, and by varying the load setting, different amounts of acoustic power are delivered to the load through the two-mic midpoint. If the two-mic measurements are accurate, the two-mic power is given by

$$\dot{W}_{2\text{mic}} = \dot{W}_{\text{res}} + \dot{W}_{\text{load}}, \quad (29)$$

where \dot{W}_{res} represents the dissipation in the resonator that occurs to the right of the two-mic midpoint. Accurate measurements of \dot{W}_{load} are easily made with the pair of microphones straddling the valve of the variable acoustic load in Fig. 1(a).¹⁶ If p_{ref}/p_m is held constant (by varying \dot{Q}_h) while \dot{W}_{load} is varied, \dot{W}_{res} is constant and a plot of $\dot{W}_{2\text{mic}}$ vs \dot{W}_{load} should be a line of slope one whose intercept at $\dot{W}_{\text{load}}=0$ is \dot{W}_{res} at p_{ref}/p_m . These data are presented in Fig. 10 for

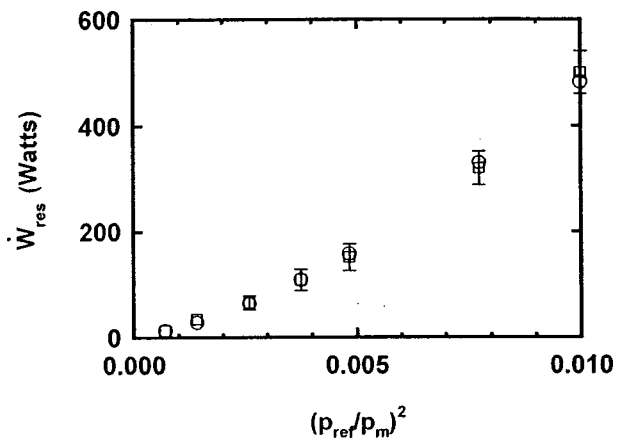


FIG. 11. \dot{W}_{res} measured (open squares) and calculated (open circles) vs $(p_{ref}/p_m)^2$. The DeltaE calculations use a relative surface roughness for the resonator of 7×10^{-5} . At low amplitudes, the error bars are smaller than the symbols.

values of p_{ref}/p_m ranging from 0.026 to 0.10. The solid lines are least-squares fits used to extract the slopes and \dot{W}_{res} . The slopes are scattered in the range 0.96–1.05 except at $p_{ref}/p_m = 0.10$ where it takes the value 0.89. This low value may be due to resonator heating caused by the large dissipation of acoustic power.

The extracted values of \dot{W}_{res} are plotted as the open squares in Fig. 11. The data are clearly not linear in $(p_{ref}/p_m)^2$ indicating enhanced dissipation in the resonator due to turbulence. This is to be expected because, as a function of p_{ref}/p_m , the peak Reynolds number in the resonator ranges from 0.4 to 1.5×10^6 and the steady-flow friction factor is nearly constant over this range.²⁹ At such large Reynolds numbers, the roughness of the resonator's inner surface is expected to play a significant role in the resonator dissipation. The open circles in Fig. 11 are DeltaE calculations²⁷ of \dot{W}_{res} using a relative surface roughness of 7×10^{-5} which corresponds to an absolute roughness of approximately 7 μm . This is considerably larger than the estimated 2- μm roughness of the metal surface. A DeltaE calculation of \dot{W}_{res} using the estimated surface roughness of 2 μm results in only 30 W less dissipation at $p_{ref}/p_m = 0.10$, or less than 6% of the total measured dissipation. This extra dissipation could also be due to unknown minor losses in the resonator. Given the approximate nature of DeltaE's turbulence algorithm and the uncertainty in using steady-flow minor loss correlations for oscillating flow, the discrepancy between the estimated surface roughness and that used in the DeltaE calculations is beyond the limit of our current knowledge.

Using this single 7- μm surface roughness for all acoustic amplitudes, we obtain good agreement between the calculated and measured \dot{W}_{res} . Therefore, we are confident that DeltaE can be used to account for the dissipation between the resonator junction and the two-mic midpoint. This small additional dissipation is added to \dot{W}_{res} , and for the rest of this article, the acoustic power flow into the resonator is reported in terms of acoustic power passing the resonator junction \dot{W}_{junc} .

Next, we consider the acoustic power dissipated in the

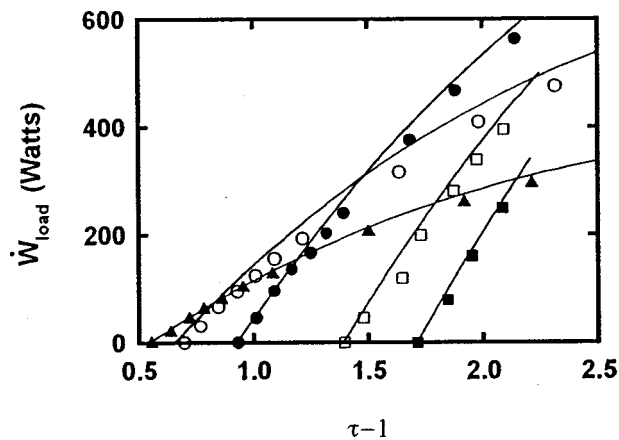


FIG. 12. \dot{W}_{load} vs $(\tau - 1)$. Measured values are given by the symbols and values calculated with DeltaE are shown as solid lines. Acoustic amplitudes are the same as those in Fig. 3 except that $p_{ref}/p_m = 0.026$ and 0.061 have been left out for clarity. Acoustic amplitude increases from left to right along the $(\tau - 1)$ axis. Agreement between the DeltaE model and the measurements is evidence that the overall dissipation in the engine is correctly accounted for in the model. The uncertainty in \dot{W}_{load} is $\pm 0.5\%$ and is independent of amplitude and $(\tau - 1)$. Typical uncertainty in $(\tau - 1)$ is $\pm 1\%$.

torus where direct measurement of the dissipation is far more difficult. The major contributors to the dissipation are viscous and thermal losses in the regenerator, inertance, and compliance; and minor losses in the inertance, compliance, jet pump, and secondary cold heat exchanger. The main cold heat exchanger, hot heat exchanger, and TBT do not dissipate a significant amount of acoustic power, but the lost energy due to irreversible heat transfer¹⁴ at the heat exchangers will be taken into account in the next section. The previous discussion of the pressure-drop phasors in the torus showed that the DeltaE model makes fairly accurate predictions of the real and imaginary parts of the pressure drops across the jet pump, regenerator, and inertance. Therefore, we will use DeltaE to compute the acoustic power dissipation in the torus elements.

C. Performance

Before using the DeltaE model to assign irreversibilities to various components, we begin this section with a summary of how the model was built up. There are two adjustable parameters, the surface roughnesses of the resonator and feedback inertance. Using the measurements of \dot{W}_{res} , a single surface roughness is assigned to the resonator which reproduces the data at all values of p_{ref}/p_m (see Fig. 11). Then, this roughness is used to extrapolate from the two-mic midpoint to the resonator junction and calculate the acoustic power flowing out of the torus \dot{W}_{junc} . The values of \dot{W}_{junc} are then used to fix the acoustic power generated by a DeltaE model of the torus. Using a single surface roughness in the feedback inertance, the torus model reproduces the pressure-drop phasors for both the jet pump and regenerator (see Fig. 4). In addition to the regenerator dissipation, the resonator and feedback dissipation provide the majority of the load on the engine, and therefore play a large role in setting T_h . As a final check of the DeltaE model, Fig. 12 presents the calculated and measured load curves, i.e., \dot{W}_{load} vs $\tau - 1$, for the

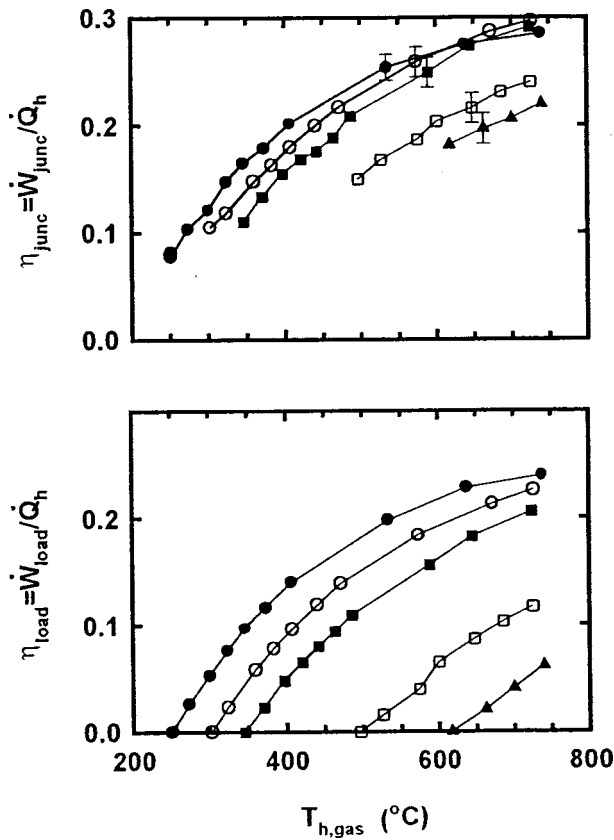


FIG. 13. Thermal efficiencies vs $T_{h,gas}$, the temperature of the helium immediately below the hot heat exchanger, for the same values of p_{ref}/p_m as in Fig. 3. $p_{ref}/p_m=0.026$ and 0.038 have been left out for clarity. Acoustic amplitude increases from left to right. The thermal efficiency is measured in two ways, i.e., in terms of the acoustic power delivered past the resonator junction (η_{junc}) or the acoustic power delivered to the load (η_{load}). The single error bar shown on each constant-amplitude η_{junc} dataset is typical of the uncertainty of every measurement in the dataset. Typical uncertainties in η_{load} and $T_{h,gas}$ are both $\pm 1\%$.

same values of p_{ref}/p_m as in Fig. 3. The good agreement provides further confidence in the ability of the DeltaE model to account for the various irreversibilities.

We now present the thermal efficiency of the engine at various acoustic amplitudes as a function of $T_{h,gas}$, the temperature of the helium immediately below the hot heat exchanger. $T_{h,gas}$ is used instead of T_h because it more closely represents the temperature which limits a practical engine due to weakening of materials in the hot zone. Figure 13 presents the engine efficiency in two ways. If the assembly is to be used in its present configuration where it is driving a load attached to the resonator, the relevant efficiency is $\eta_{load} = \dot{W}_{load}/\dot{Q}_h$. If it is scaled up to a size where the resonator dissipation is a small fraction of the total dissipation or if it is one of many engines driving a single resonator, the relevant efficiency is $\eta_{junc} = \dot{W}_{junc}/\dot{Q}_h$. We will focus on the latter, as our future plans include multiple scaled-up engines on a single large resonator.

The η_{junc} data show that for $p_{ref}/p_m \approx 0.06$ and $T_{h,gas} \approx 725$ °C, the engine is converting \dot{Q}_h to acoustic power with a conversion efficiency of 0.30. Expressed in a different way, the engine is operating with 41% of the theoretical maximum efficiency, the Carnot efficiency. Here, the Carnot

efficiency is based on the estimated temperature of the Ni–Cr in the hot heat exchanger and the average temperature of the cooling water in the main cold heat exchanger. This represents more than a 50% increase over the best standing-wave thermoacoustic engines.¹² At this operating point, the engine is delivering 710 W past the resonator junction. As the acoustic amplitude is increased to $p_{ref}/p_m=0.10$ where the power density is higher, η_{junc} falls off to 0.22 at $T_{h,gas}=725$ °C with the engine delivering 890 W past the resonator junction.

Next, we use a combination of direct measurements and DeltaE calculations to determine where the major irreversibilities occur and why η_{junc} falls off at higher acoustic amplitude. To place all irreversibilities on an equal footing, we use the concept of exergy or available work,¹⁴ which is a measure of the work-equivalent “value” of energy when a thermal reservoir at ambient temperature is freely available. Heat \dot{Q} at temperature T carries exergy $\dot{X} = \dot{Q}(1 - T_0/T)$, where T_0 is the ambient temperature. A thermoacoustic wave carries $\dot{X} = (T_0/T)\dot{W} + (1 - T_0/T)\dot{H}$,³⁵ where \dot{H} is the total power flow.¹¹ In a wide duct $\dot{X} = \dot{W}$. In an ideal regenerator ($r_h \ll \delta_\kappa$), $\dot{H} = 0$, so $\dot{X} = (T_0/T)\dot{W}$. In a realistic regenerator, \dot{H} must be taken into account. In a thermoacoustic-Stirling engine, there are three basic mechanisms for destroying exergy: heat flow \dot{Q} across a finite temperature difference ($T_1 \rightarrow T_2$) with $\dot{X}_{lost} = \dot{Q}T_0(T_1 - T_2)/(T_1T_2)$; dissipation of acoustic power \dot{W}_{diss} at temperature T with $\dot{X}_{lost} = (T_0/T)\dot{W}_{diss}$; and regenerator ineffectiveness which is a combination of acoustic power dissipation at temperature T and “thermoacoustic heat pumping” due to $\dot{H} \neq 0$. In the last case, $\dot{X}_{lost} = \dot{X}_h - \dot{X}_c$ where \dot{X}_h and \dot{X}_c are the thermoacoustic exergy fluxes at the hot and cold faces of the regenerator.

Table II lists different elements of the engine, what physical process causes the loss of exergy, how it was determined, and what fraction of the total input exergy this process is responsible for destroying. The final two entries in the table list the total input exergy and what fraction cannot be accounted for in the analysis. The use of exergy allows direct comparison of the importance of different irreversibilities. The increase in amplitude from $p_{ref}/p_m=0.061$ to 0.10 shows several expected trends. Losses due to conduction heat leaks decrease in their relative importance as the acoustic power density grows. The losses in the regenerator increase, but not as fast as $(p_{ref}/p_m)^2$. Since the Reynolds number in the regenerator is low, the dissipation is proportional to a weighted average of $|U_1|^2$ within the regenerator. As p_{ref}/p_m increases, $|U_{1,c}|$ remains roughly constant due to the amplitude dependent R_{jp} . However, $|U_{1,h}|$ increases with amplitude due to the compliance of the regenerator, and the magnitude of the loss scales roughly as $(|U_{1,c}|^2 + |U_{1,h}|^2)/2$. Losses in the feedback inductance grow in their relative importance because, at these amplitudes, the minor losses and turbulence cause the acoustic dissipation to grow as $(p_{ref}/p_m)^3$. Also, the relative importance of residual streaming in the TBT seems to decrease, but the cause of this is presently unknown.

Table II also shows the areas where basic research into the loss mechanisms can provide the fastest improvements in

TABLE II. Major causes of lost exergy, sorted according to engine element and physical process. The losses are either directly measured or calculated using DeltaE. The DeltaE model is built up according to the principles outlined at the beginning of Sec. V C. The final two entries in the table are the total input exergy at the hot heat exchanger and what fraction of this cannot be accounted for in the analysis.

Element	Process	Method	$p_{\text{ref}}/p_m = 0.061$ $T_{h,\text{gas}} = 725\text{ }^\circ\text{C}$		$p_{\text{ref}}/p_m = 0.10$ $T_{h,\text{gas}} = 725\text{ }^\circ\text{C}$	
			$\dot{X}_{\text{lost}}(W)$	Fraction	$\dot{X}_{\text{lost}}(W)$	Fraction
Regenerator	Viscous/Thermal loss	DeltaE	238	0.14	393	0.13
	Heat leak	Measured	163	0.09	172	0.06
Feedback inertance	Minor loss	DeltaE	62	0.04	296	0.10
	Viscous/Thermal loss	DeltaE	36	0.02	145	0.05
Thermal buffer tube	Residual streaming	Measured	82	0.05	25	0.01
	Radiation	Measured	69	0.04	78	0.03
	Metallic conduction	Measured	52	0.03	55	0.02
	Boundary-layer transport	DeltaE	7	<0.01	18	<0.01
	Flow straightener	DeltaE	2	<0.01	10	<0.01
	Heat leak	Measured	82	0.05	87	0.03
Insulation	Heat leak	Measured	82	0.05	87	0.03
	Temperature difference	Measured	57	0.03	181	0.06
Main cold heat exchanger	Viscous loss	DeltaE	4	<0.01	12	<0.01
	Temperature difference	Measured	43	0.02	114	0.04
Hot heat exchanger	Viscous loss	DeltaE	4	<0.01	11	<0.01
	Temperature difference	Measured	43	0.02	114	0.04
Sec. cold heat exchanger	Minor/Viscous loss	DeltaE	34	0.02	144	0.05
Jet pump	Minor/Viscous loss	DeltaE	30	0.02	130	0.04
Resonator and load	Delivered power	Measured	710	0.41	890	0.30
Input exergy	$(1 - T_{\text{hhx}}/T_{\text{water}})\dot{Q}_h$	Measured	1724	1.00	2968	1.00
Unaccounted \dot{W}_{lost}			44	0.03	200	0.07

efficiency. The screen-bed regenerator used in this engine could be replaced by a parallel-plate regenerator which would have lower viscous losses while still providing the necessary regenerative heat exchange. The smaller viscous resistance would also allow the feedback inertance and compliance to be redesigned in such a way that viscous and minor losses in those parts would be reduced. The technical challenge is the construction of parallel plates with uniform spacing on the order of $75\text{ }\mu\text{m}$ and an acceptable level of heat leak. Also, basic research into minor losses in oscillating flows might provide insight into how these losses occur and methods to reduce them.

VI. CONCLUSION

We have constructed a new type of thermoacoustic engine that is based on traveling-wave phasing and a Stirling-like thermodynamic cycle. In designing and building this engine, we have followed the basic traveling-wave principle described by Ceperley,^{4,6} but with many improvements and additional elements that are necessary to achieve high efficiency. Our engine uses an ideally reversible acoustic network, which is much shorter than $1/4$ wavelength, to feed acoustic power to the cold end of the regenerator and convert standing-wave phasing in the acoustic resonator to the necessary traveling-wave phasing while maintaining $|p_{1,c}/U_{1,c}| \gg \rho c/A$. In comparison with Ceperley, our network naturally creates a large value of $|p_{1,c}/U_{1,c}|$ without large changes in duct diameter. To achieve the high efficiencies reported in this article, two types of acoustic streaming that were not foreseen by Ceperley have been suppressed. Gedeon streaming is eliminated by the use of a jet pump that relies on the asymmetry of hydrodynamic end effects, and Rayleigh streaming is reduced by appropriately tapering the TBT.

Measurements show that the first-order dynamics in the torus section of the engine are well understood, but that we have only a qualitative understanding of many of the nonlinear effects in the engine. To allow for quantitative design in the future, several areas require further research. Basic research into minor losses in oscillating flow is required to place the incorporation of these losses on firmer ground. The magnitude of Gedeon streaming needs further study so that jet pumps, or other means of suppressing this time-averaged flow, can be appropriately designed. Also, more careful measurements on Rayleigh streaming in the thermal buffer tube are required to determine how turbulence modifies this type of streaming.

At the most efficient operating point, the engine delivers 710 W to its resonator with an efficiency of 0.30 which corresponds to 41% of the Carnot efficiency. At the most powerful operating point, the engine delivers 890 W to its resonator with an efficiency of 0.22. We have identified the irreversible processes and sources of lost work. This analysis suggests the path of future research on thermoacoustic-Stirling hybrid engines. Although some of the phenomena are not yet fully understood, and further improvement is possible, the efficiency is already excellent: more than a 50% increase over the best standing-wave thermoacoustic engines.

ACKNOWLEDGMENTS

We thank D. L. Gardner, C. Espinoza, and R. Rockage for their expert assistance in the construction of the engine, and the Office of Basic Energy Sciences in the U.S. DOE for financial support.

- ¹G. Walker, *Stirling Engines* (Clarendon, Oxford, 1960).
- ²R. Radebaugh, "A review of pulse tube refrigeration," *Adv. Cryog. Eng.* **35**, 1191–1205 (1990).
- ³C. D. West, *Liquid Piston Stirling Engines* (Van Nostrand Reinhold, New York, 1983).
- ⁴P. H. Ceperley, "A pistonless Stirling engine—the traveling wave heat engine," *J. Acoust. Soc. Am.* **66**, 1508–1513 (1979).
- ⁵T. Yazaki, A. Iwata, T. Maekawa, and A. Tominaga, "Traveling wave thermoacoustic engine in a looped tube," *Phys. Rev. Lett.* **81**, 3128–3131 (1998).
- ⁶P. H. Ceperley, "Gain and efficiency of a short traveling wave heat engine," *J. Acoust. Soc. Am.* **77**, 1239–1244 (1985).
- ⁷David Gedeon, "DC gas flows in Stirling and pulse-tube cryocoolers," in *Cryocoolers 9*, edited by R. G. Ross (Plenum, New York, 1997), pp. 385–392.
- ⁸J. R. Olson and G. W. Swift, "Acoustic streaming in pulse tube refrigerators: Tapered pulse tubes," *Cryogenics* **37**, 769–776 (1997).
- ⁹Y. L. Ju, C. Wang, and Y. Zhou, "Dynamic experimental study of the multi-bypass pulse tube refrigerator with two-bypass tubes," *Adv. Cryog. Eng.* **43**, 2031–2037 (1998).
- ¹⁰A. Ravex, J. M. Poncet, I. Charles, and P. Bleuze, "Development of low frequency pulse tube refrigerators," *Adv. Cryog. Eng.* **43**, 1957–1964 (1998).
- ¹¹G. W. Swift, "Thermoacoustic engines," *J. Acoust. Soc. Am.* **84**, 1145–1180 (1988).
- ¹²To our knowledge, the highest thermal efficiency in a standing-wave engine is 0.18, reported by C. Jin, based on acoustic power delivered from the engine to the resonator, using the apparatus described by K. M. Godshalk *et al.*, *Adv. Cryog. Eng.* **41**, 1411–1418 (1996). Comparable efficiency has been obtained with the much larger standing-wave engine at Cryenco, Inc. described in <http://lib-www.lanl.gov/la-pubs/00412750.pdf>.
- ¹³S. Backhaus and G. W. Swift, "A thermoacoustic-Stirling heat engine," *Nature (London)* **399**, 335–338 (1999).
- ¹⁴Adrian Bejan, *Advanced Engineering Thermodynamics*, 2nd ed. (Wiley, New York, 1997).
- ¹⁵A. J. Organ, *Thermodynamics and Gas Dynamics of the Stirling Cycle Machine* (Cambridge University Press, Cambridge, U.K., 1992).
- ¹⁶A. M. Fusco, W. C. Ward, and G. W. Swift, "Two-sensor power measurements in lossy ducts," *J. Acoust. Soc. Am.* **91**, 2229–2235 (1992).
- ¹⁷W. D. Klopp, Inconel Alloy 625. *Aerospace Structural Metals Handbook*, Code 4117, July 1993, Metals and Ceramics Information Center (1997).
- ¹⁸Ohio Semitronics, Inc., 4242 Reynolds Dr., Hilliard, OH 43026.
- ¹⁹I. E. Idelchik, *Handbook of Hydraulic Resistance*, 3rd ed. (Begell House, New York, 1996).
- ²⁰G. W. Swift, D. L. Gardner, and S. Backhaus, "Acoustic recovery of lost power in pulse tube refrigerators," *J. Acoust. Soc. Am.* **105**, 711–724 (1999).
- ²¹M. Iguchi, M. Ohmi, and K. Maegawa, "Analysis of free oscillating flow in a U-shaped tube," *Bull. JSME* **25**, 1398 (1982).
- ²²Endevco Corporation, 30700 Rancho Viejo Road, San Juan Capistrano, CA 92675.
- ²³L. E. Kinsler, A. R. Frey, A. B. Coppens, and J. V. Sanders, *Fundamentals of Acoustics* (Wiley, New York, 1982).
- ²⁴W. M. Kays and A. L. London, *Compact Heat Exchangers* (McGraw-Hill, New York, 1964).
- ²⁵P. Kittel, "Ideal orifice pulse tube refrigerator performance," *Cryogenics* **32**, 843–844 (1992).
- ²⁶G. W. Swift and W. C. Ward, "Simple harmonic analysis of regenerators," *J. Thermophys. Heat Transfer* **10**, 652–662 (1996).
- ²⁷W. C. Ward and G. W. Swift, "Design environment for low amplitude thermoacoustic engines (DeltaE)," *J. Acoust. Soc. Am.* **95**, 3671–3672 (1994). Fully tested software and users guide available from Energy Science and Technology Software Center, US Department of Energy, Oak Ridge, Tennessee. To review DeltaE's capabilities, visit the Los Alamos thermoacoustics web site at <http://www.lanl.gov/thermoacoustics/>. For a beta-test version, contact ww@lanl.gov (Bill Ward) via Internet.
- ²⁸To obtain the DeltaE input file used to model the engine, visit <http://www.lanl.gov/projects/thermoacoustics/Tashe.out>.
- ²⁹R. W. Fox and A. T. McDonald, *Introduction to Fluid Mechanics* (Wiley, New York, 1985).
- ³⁰V. L. Streeter, *Handbook of Fluid Dynamics* (McGraw-Hill, New York, 1961).
- ³¹M. Ohmi and M. Iguchi, "Critical Reynolds number in an oscillating pipe flow," *Bull. JSME* **25**, 165 (1982).
- ³²Unifrax Corp., 2351 Whirlpool St., P.O. Box 156, Niagara Falls, NY 14302.
- ³³M. A. Lewis, T. Kuriyama, F. Kuriyama, and R. Radebaugh, "Measurement of heat conduction through stacked screens," *Adv. Cryog. Eng.* **43**, 1611–1618 (1998).
- ³⁴C. F. Hickey. 304 Stainless steel. *Aerospace Structural Metals Handbook*, Code 1303, March 1973, Metals and Ceramics Information Center (1997).
- ³⁵G. W. Swift, *Thermoacoustics: A unifying perspective for some engines and refrigerators* (1999 draft available at <http://www.lanl.gov/thermoacoustics/Book/index.html>).